

1
2
3
4
5
6
7
8
9
10
11
12
13
14
15
16
17
18
19
20
21
22
23
24
25
26
27
28
29
30
31

Constraining plateau uplift in southern Africa by combining thermochronology, sediment flux, topography, and landscape evolution modeling

Jessica R. Stanley¹, Jean Braun^{2,3}, Guillaume Baby⁴, François Guillocheau⁵, Cécile Robin⁵, Rebecca M. Flowers⁶, Roderick Brown⁷, Mark Wildman⁷, Romain Beucher⁸

¹ Department of Geological Sciences, University of Idaho, 875 Perimeter Dr MS3022, Moscow ID 83843, USA.

² Helmholtz Centre Potsdam, GFZ German Research Center for Geosciences, Telegrafenberg Building A27, 14473 Potsdam, Germany.

³ Institut für Erd- und Umweltwissenschaften, Universität Potsdam, 14476 Potsdam, Germany.

⁴ Université de Paris, Institut de Physique du Globe de Paris, CNRS, F-75005, Paris, France.

⁵ Université de Rennes 1, CNRS, Géosciences Rennes - UMR 6118, 35000 Rennes, France.

⁶ Department of Geological Sciences, University of Colorado Boulder, UCB399, Boulder CO 80309, USA.

⁷ School of Geographical and Earth Sciences, University of Glasgow, Glasgow, Scotland.

⁸ Research School of Earth Sciences, The Australian National University, Canberra ACT 2600, Australia.

Corresponding author: Jessica R. Stanley (jessicastanley@uidaho.edu)

Key Points:

- Hypotheses for southern African Plateau uplift are tested using large scale landscape model inversions
- Comparison of models to published thermochronology, sediment flux volumes, and topography highlight two suitable uplift histories
- Data cannot distinguish between these two models, which have different geodynamic implications, but do highlight areas for future work

32 **Abstract**

33 The uplift of the southern African Plateau is often attributed to mantle processes, but there are
34 conflicting theories for the specific timing and drivers of topographic development. Evidence for
35 most proposed plateau development histories is derived from continental erosion histories,
36 marine stratigraphic architecture, or landscape morphology. Here we use a landscape evolution
37 model to integrate these three types of data for southern Africa, including a large dataset of low
38 temperature thermochronology, sediment flux rates to surrounding marine basins. We explore
39 three main hypotheses for surface uplift: 1) southern Africa was already elevated at the time of
40 Gondwana breakup, 2) uplift and continental tilting occurred in the mid-Cretaceous, or 3) uplift
41 occurred in the mid to late Cenozoic. We test which of these three intervals of plateau
42 development are plausible by using an inversion method to constrain the range in erosional and
43 uplift model parameters that can best reproduce the observed data. Results indicate two families
44 of uplift histories are most compatible with the data. Both have limited initial topography with
45 some topographic uplift and continental tilting starting in the east at ~95 Ma. In one acceptable
46 scenario, nearly all of the topography, ~1400 m, is created at this time with little Cenozoic uplift.
47 In the other acceptable scenario, only ~500 m of uplift occurs in the mid-Cretaceous with another
48 ~850 m of uplift in the mid-Cenozoic. The two model scenarios have different geodynamic
49 implications, which in the future could be evaluated by direct comparison between geodynamic
50 and landscape model predictions.

51 **Plain Language Summary**

52 How the southern African Plateau and its high elevations formed is disputed. The plateau is
53 located far from tectonic plate boundaries, and many have suggested that processes below the
54 crust are responsible for plateau uplift. Here, we use a wide range of data that documents the
55 long term erosion history of the plateau and a landscape evolution model to test proposed uplift
56 histories. Model results show two plateau uplift histories that can adequately match the data. One
57 suggests that all the plateau was uplifted rapidly ~90-100 million years ago. The other suggests
58 two phases of uplift, one ~90-100 million years ago, and a second ~25-35 million years ago. We
59 cannot indicate which one is correct with the data that we included, but the results have different
60 implications for processes occurring in the deep earth.

61

62 **1. Introduction**

63 The southern African Plateau is a dominant feature of African topography, but there is
64 still debate about when and how it formed. Topographic heights reach >3000 m, with an average
65 elevation of ~1000 m in the predominantly low relief plateau interior. The margins of the plateau
66 drop through higher relief regions to the coastal plain (Figure 1). The long wavelength
67 topographic high in absence of collisional tectonism combined with Cretaceous kimberlite
68 activity and a large low shear seismic velocity province (LLSVP) in the deep mantle below
69 southern Africa have led many to suggest uplift related to mantle processes. Potential
70 mechanisms contributing to uplift include lithospheric heating and modification related to
71 kimberlite magmatism or delamination (e.g., Bell et al., 2003; Hu et al., 2018; Stanley et al.,
72 2013; Tinker et al., 2008b), small scale convection induced when the African plate became stable
73 with respect to the underlying mantle (e.g., Burke, 1996; Burke & Gunnell, 2008), and dynamic
74 topography associated with the LLSVP (e.g., Braun et al., 2014; Gurnis et al., 2000; Lithgow-
75 Bertelloni & Silver, 1998). Given that surface uplift may be related to LLSVP development,
76 better constraints on the timing of uplift could provide additional information on the nature and
77 development of this deep seismic anomaly and mantle processes that may cause southern
78 Africa's anomalous elevations (e.g., Gurnis et al., 2000).

79 Overall, three main intervals have been proposed for when most of the uplift occurred in
80 southern Africa (summarized in Table 1). First, the plateau may already have been elevated
81 prior to 130 Ma at the time of Gondwana breakup due to processes that occurred prior to or
82 associated with supercontinent breakup. Hypothesized geodynamic mechanisms to achieve uplift
83 at this time include thermal uplift and crustal thickening due to large igneous provinces (LIPs,
84 e.g., Cox, 1989), isostatic rebound after dynamic subsidence and deposition of the continental
85 Karoo Basin (Pysklywec & Mitrovica, 1999), and inherited topography (Doucouré & de Wit,
86 2003). Most of the supporting evidence for pre-130 Ma uplift is based on the morphology of rift
87 flank uplifts, their erosion, and models for their evolution (e.g., Gilchrist et al., 1994; Gilchrist &
88 Summerfield, 1990; Van Der Beek et al., 2002). Second, uplift may have occurred 100-80 Ma.
89 This timing is supported by a major pulse of continental erosion detected by thermochronology
90 and marine sediment flux (e.g., Baby et al., 2020; Flowers & Schoene, 2010; Gallagher &
91 Brown, 1999b; Guillocheau et al., 2012; Kounov et al., 2013; Stanley et al., 2013; Tinker et al.,
92 2008a; Wildman et al., 2015). Many geodynamic mechanisms have been proposed to generate

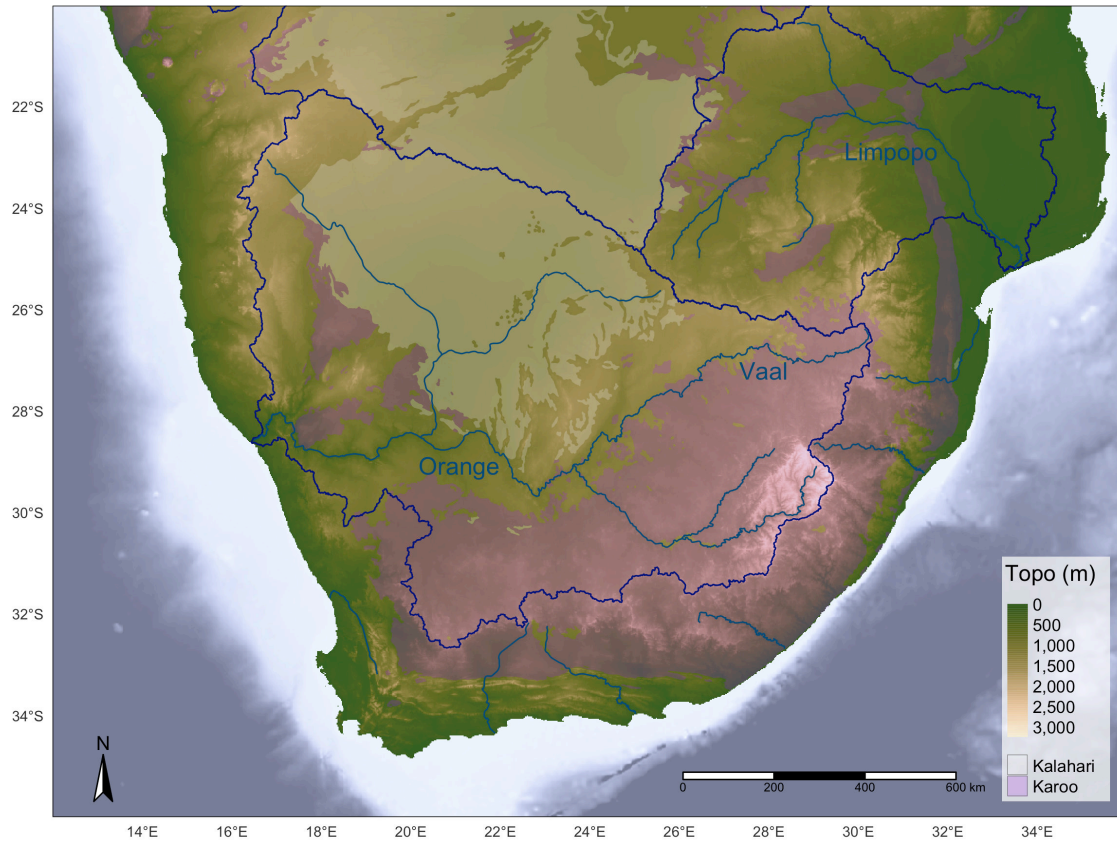


Figure 1. Topography and simplified post-300 Ma geology for southern Africa. Dark blue lines show the main drainage divides. Purple shading denotes the extent of Permian to Jurassic Karoo sedimentary basin, Jurassic Karoo lavas and sills, and early Cretaceous Etendeka Lavas, while the light shading shows the extent of thin Cenozoic Kalahari basin deposits.

94 plateau uplift at this time (see Table 1), but the two most commonly invoked are dynamic
95 topography due to the LLSVP (e.g., Braun et al., 2014; Lithgow-Bertelloni & Silver, 1998) or
96 changes in lithospheric buoyancy associated with kimberlite magmatism (e.g., Hu et al., 2018;
97 Stanley et al., 2013; Tinker et al., 2008b). Continent-wide tilting has been shown to be important
98 during this phase (Braun et al., 2014), and potentially caused by either motion of the African
99 plate onto a dynamic topography high above the LLSVP (Braun et al., 2014), or delamination
100 and/or lithospheric changes buoyancy with the east to west progression of kimberlites (Bell et al.,
101 2003; Hu et al., 2018). Finally, uplift may have occurred after ~30 Ma. This is usually attributed
102 to dynamic topography and small scale convection in the upper mantle (e.g., Al-Hajri et al.,
103 2009; Burke, 1996), though others suggest that the LLSVP developed during this period (Al-
104 Hajri et al., 2009; Gurnis et al., 2000). Evidence for Cenozoic uplift is dominantly based on
105 mapping of planation surfaces, (e.g., Burke, 1996; Burke & Gunnell, 2008; Partridge & Maud,
106 1987; Paul et al., 2014; G. G. Roberts & White, 2010), river profile analysis (e.g., Paul et al.
107 2014; Roberts & White, 2010), or stratigraphic data (tilting and truncation of the margin, forced
108 regressive wedges, e.g. Baby et al., 2018). Some authors (Baby et al., 2020) suggested a two
109 steps-uplift of the southern Africa Plateau, at 93-70 (tilting of the plateau) and 25-15 Ma (Indian
110 Ocean side only).

111 The timing and patterns of uplift are key for resolving the driving mechanisms, but
112 because topographic uplift is difficult to discern directly from the continental rock record there
113 remains discussion on how extensive surface uplift was during each of these three intervals.
114 There are rarely direct proxies for paleoelevation, and commonly surface uplift is inferred based
115 on the assertion that topographic uplift generates relief which triggers an erosional response that
116 is easier to detect in the rock record. Recent work using thermochronology (Brown et al., 2014;
117 Green et al., 2017; Kounov et al., 2013; Stanley et al., 2013, 2015; Stanley & Flowers, 2020;
118 Wildman et al., 2015, 2016, 2017) and quantifying sediment flux to the marine basins (Baby et
119 al., 2020; Baby, Guillocheau, Boulogne, et al., 2018; Baby, Guillocheau, Morin, et al., 2018;
120 Guillocheau et al., 2012; Said et al., 2015) combined with extensive previous work (Belton &
121 Raab, 2010; Brown et al., 2002; Flowers & Schoene, 2010; Gallagher & Brown, 1999a, 1999b;
122 Kounov et al., 2009; Raab et al., 2002; Rouby et al., 2009; Tinker et al., 2008a, 2008b) now
123 gives a fairly complete picture of the long term erosion and sedimentation history in southern
124 Africa. Together these records show a substantial pulse of continental erosion and associated

125 marine sedimentation in the Cretaceous with little erosion after that time. This has led many to
126 suggest that the plateau was uplifted in the Cretaceous with limited subsequent activity (e.g.,
127 Brown et al., 2002; Flowers & Schoene, 2010; Stanley et al., 2015; Tinker et al., 2008b;
128 Wildman et al., 2017), but the magnitude of surface uplift required to drive this erosion phase is
129 not known. Additionally, the morphology of the landscape should contain signatures of the uplift
130 history, and some have argued for more recent uplift of the plateau based dominantly on
131 geomorphic observations. These include the postulated ages of geomorphic planation surfaces
132 (e.g., Burke, 1996; Burke & Gunnell, 2008; King, 1942, 1950; Partridge et al., 2010; Partridge &
133 Maud, 1987) as well as river profile inversion work (Paul et al., 2014; G. G. Roberts & White,
134 2010; Rudge et al., 2015). However, the time or rate of formation of some of these geomorphic
135 features is difficult to constrain.

136 Surface process models that focus on some or all of the landscape can be used to derive
137 more quantitative estimates of how topographic change relates to erosion history and geomorphic
138 features. Previous work linking topography and AFT data from the southwest coast indicated the
139 existence of a pre-breakup drainage divide similar to the present-day divide in this area (Van Der
140 Beek et al., 2002). Block landscape models aimed at reproducing the sediment flux to the west
141 coast marine basins showed that continent-scale tilting during early Late Cretaceous uplift was
142 necessary to reproduce the observations (Braun et al., 2014). Additional modelling of a generic
143 continent subjected to a propagating wave of dynamic topography argued that the modelled
144 sedimentary architecture was consistent with Cretaceous sedimentary archives from southern
145 Africa (Ding et al., 2019). Modelling efforts focused on river profile shape have taken this
146 approach a step further by comparing modeled and observed river profiles to invert for uplift
147 histories that suggest that the high topography was developed in the last 30-40 Ma (Paul et al.,
148 2014; G. G. Roberts & White, 2010; Rudge et al., 2015). This is an interesting methodology
149 because it allows the systematic exploration of a wide range of uplift parameters, but the absolute
150 timing of the uplift histories it yields depends on an assumed value for rock erodibility, which is
151 difficult to constrain. All of these methods have only focused on one main piece of the erosion
152 history or landscape, yielding important insights into aspects of the southern African topographic
153 history but leading to incomplete and sometimes conflicting results between modeling
154 approaches.

Timing	Geodynamic Mechanism	Evidence
Before or during Gondwana breakup (> 130 Ma)	<ul style="list-style-type: none"> ▪ Thermal uplift and crustal thickening associated with LIP activity (Cox, 1989) ▪ Isostatic rebound after dynamic subsidence and deposition of the Karoo basin (Pysklywec & Mitrovica, 1999) ▪ Inherited Paleozoic topography (Doucouré & de Wit, 2003) ▪ Flexural uplift from far field plate stresses (A. E. Moore, 1999; A. E. Moore et al., 2009) 	<ul style="list-style-type: none"> ▪ Major phase of cooling in AFT thermochronology studies around the margins just after rifting (Brown et al., 1990, 2002; Gallagher & Brown, 1999a; Tinker et al., 2008b; Wildman et al., 2015, 2016) ▪ Models of escarpment retreat developed in S. Africa suggest some topography at breakup (Gilchrist et al., 1994; Gilchrist & Summerfield, 1990) and a pre-existing topographic divide (Van Der Beek et al., 2002) ▪ Radial drainages around LIPs (Cox, 1989)
Mid-Cretaceous (110-80 Ma)	<ul style="list-style-type: none"> ▪ Dynamic topography due to the LLSVP in the deep mantle (Braun et al., 2014; Lithgow-Bertelloni & Silver, 1998) ▪ Changes to the lithospheric density structure (Bell et al., 2003; Stanley et al., 2013), long lived plume tails (Nyblade & Sleep, 2003), and/or delamination (Hu et al., 2018) associated with kimberlite magmatism ▪ Pressure driven flow in the asthenosphere (Colli et al., 2014) ▪ Flexural uplift from far field plate stresses (Moore, 1999; Moore et al., 2009) ▪ Agulhas LIP off the S coast at ~90 Ma (M. de Wit, 2007) 	<ul style="list-style-type: none"> ▪ Phase of cooling seen in AFT (Brown et al., 2002; Gallagher & Brown, 1999a, 1999b; Kounov et al., 2009; Tinker et al., 2008b; Wildman et al., 2015) and AHe (Flowers & Schoene, 2010; Kounov et al., 2013; Stanley et al., 2013, 2015; Stanley & Flowers, 2020; Wildman et al., 2017) ▪ Major pulse of sediment delivered to the marine basins off the western and southern coasts (Baby et al., 2020; Guillocheau et al., 2012; Rouby et al., 2009; Tinker et al., 2008a). ▪ Geometric evidence from offshore forced regressive wedges, margin tilting, and incised valleys (Baby et al. 2020)
Mid- to Late Cenozoic (<35 Ma)	<ul style="list-style-type: none"> ▪ Small scale convection in the upper mantle due to the slowing of African plate at ~30 Ma (Burke, 1996; Burke & Gunnell, 2008; Burke & Wilson, 1972) ▪ Dynamic topography due to density variations in the upper mantle and/or the LLSVP (Al-Hajri et al., 2009; Gurnis et al., 2000; Lithgow-Bertelloni & Silver, 1998; Moucha & Forte, 2011; Paul et al., 2014; Winterbourne et al., 2009) Flexural uplift from far field plate stresses (Moore, 1999; Moore et al., 2009) 	<ul style="list-style-type: none"> ▪ Large scale correlation of geomorphic surfaces (Burke & Gunnell, 2008; King, 1942; Partridge & Maud, 1987) ▪ River profiles and models of their formation through time (Paul et al., 2014; G. G. Roberts & White, 2010; Rudge et al., 2015) ▪ Terraces on the lower Orange River (Dauteuil et al., 2015) ▪ Geometric evidence from offshore forced regressive wedges and margin tilting (Baby et al. 2020) ▪ Inferred cooling phase on the southern coast (Green et al., 2017)

Table 1. Proposed geodynamic mechanisms and evidence for proposed stages of uplift

155
156157 Here we aim to take advantage of the many datasets quantifying the erosion history of
158 southern Africa and combine them with topographic metrics to explore how much uplift

159 occurred during each of the three proposed periods of plateau development using landscape
160 evolution model inversions. By using thermochronology dates, marine sediment flux volumes,
161 and topography we aim to quantify the surface uplift histories that are most compatible with all
162 the observations. To do this, we use a highly efficient forward landscape evolution model,
163 FastScape (Braun & Willett, 2013), to predict erosion and topography from a wide range of
164 uplift histories and erosional parameters. Model outputs are directly compared with observations,
165 and we use an inversion optimization scheme to isolate the uplift histories that best match the
166 data. Resulting good fit histories give quantitative estimates of uplift magnitudes and rates
167 through time that are compared to proposed geodynamic mechanisms for uplift. Results yield
168 insights into the links between topographic change and erosion in southern Africa that could be
169 compared directly with the outputs of geodynamic models in the future.

170

171 **2. Background**

172 2.1 Geomorphic and Geologic setting

173 Combined with the eastern African Plateau and anomalously shallow bathymetry in the
174 southeast Atlantic Ocean, southern Africa forms a part of the “African superswell” (Nyblade &
175 Robinson, 1994) of high topography and bathymetry. Unlike the eastern African Plateau and the
176 other topographic swells in north and central Africa, southern Africa does not have active
177 volcanism. It forms a broad (>1200 km wide) plateau with the highest elevations around the rim
178 of the plateau forming what has been termed the “great escarpment” (Fig 1). The escarpment sits
179 generally 100-200 km inboard of the coast and is often interpreted as a resulting from the retreat
180 of set of flexural rift shoulders (e.g., Braun, 2018; ten Brink & Stern, 1992; Gilchrist et al., 1994)
181 that separates the higher relief, more heavily eroded coastal plains from the plateau interior. At
182 present, the interior of the plateau is almost entirely drained by the west-draining Orange River
183 system. Evidence from much higher sediment flux rates on the west coast (e.g., Baby et al.,
184 2020; Guillocheau et al., 2012; Tinker et al., 2008a) and the locations of detrital diamond sources
185 (Bluck et al., 2005; Nakashole et al., 2018; Phillips et al., 2018; Phillips & Harris, 2009) show
186 that the plateau has been west-draining since Gondwana breakup. Drainage reconstructions
187 suggest some reorganization of plateau drainage since the Cretaceous, but most suggest the
188 dominance of large, west-draining river systems (R. Dingle & Hendry, 1984; Partridge & Maud,
189 1987; Stevenson & McMillan, 2004; M. C. J. de Wit, 1999).

190 Geologically, southern Africa is a continental shield composed of dominantly
191 Precambrian lithosphere. The Archean Kaapvaal and Zimbabwe cratons are sutured by the
192 Archean to Paleoproterozoic Limpopo Belt and surrounded by several other Proterozoic mobile
193 belts. This crystalline basement is overlain by several locally preserved Precambrian sedimentary
194 and volcanic sequences. In the south, the Paleozoic Cape Supergroup was folded into the Cape
195 Fold Belt (~275 Ma to ~250 Ma, Hansma et al., 2016). Much of the Cape Fold Belt consists of
196 quartzites that are resistant to erosion (Scharf et al., 2013). As a whole these Precambrian and
197 Paleozoic rock units are relatively resistant to erosion.

198 The Karoo sedimentary sequences were deposited from ~300 Ma to ~180 Ma. They once
199 covered much of southern Africa with substantial thickness still preserved today (Fig 1). Their
200 deposition was partly contemporaneous with the development of the Cape Fold Belt and in
201 places they are deformed by this event (Linol & De Wit, 2016). These sediments were deposited
202 either in a foreland basin related to this orogeny (Catuneanu et al., 2005) or due to dynamic
203 subsidence induced by subduction to the south (Pysklywec & Mitrovica, 1999). The base of the
204 Karoo Supergroup consists of marine glacial sediments (Dietrich & Hofmann, 2019) and
205 turbiditic to continental deposits (Catuneanu et al., 2005; Johnson et al., 1996). Sedimentation
206 terminated with the eruption of the ~183 Ma basalts of the Karoo Large Igneous Province (LIP)
207 (Duncan et al., 1997; Jourdan et al., 2008). In addition to the basalts, an extensive network of
208 dolerite sills was emplaced within the entire Karoo sequence, concurrent with the eruption of the
209 basalts at the surface (Svensen et al., 2012). The maximum preserved thickness of the Karoo
210 Supergroup is up to 6 km (Scheiber-Enslin et al., 2015), with up to 1.7 km of basalt preserved in
211 the Lesotho remnant (Marsh et al., 1997). The clastic sediments of the Karoo sequence are much
212 less resistant to erosion than the underlying Precambrian rocks and Cape Fold Belt (e.g., Braun et
213 al., 2014).

214 Post-Karoo units include the relatively thin poorly-dated Kalahari sediments (Early
215 Cretaceous? to Cenozoic) in the north, the igneous rocks of the ~132 Ma (Renne et al., 1996)
216 Etendeka LIP in western Namibia and South Africa, and many Cambrian to Paleogene
217 kimberlites. There are two major pulses of kimberlite magmatism in the Jurassic through
218 Cretaceous, with pulses peaking at ~90 Ma and ~120 Ma (Jelsma et al., 2004).

219

220 2.2 Constraints on the erosion history of southern Africa

221 2.2.1 Offshore constraints from stratigraphy

222 Terrigenous sedimentary flux shed off the continent has been quantified for the western
223 and southern margins of southern Africa based on seismic lines and borehole data (Baby et al.,
224 2020; Baby, Guillocheau, Boulogne, et al., 2018; Baby, Guillocheau, Morin, et al., 2018;
225 Guillocheau et al., 2012; Rouby et al., 2009; Tinker et al., 2008a). This includes quantifying the
226 siliciclastic component by correcting for in-situ carbonate production and porosity (Baby et al.,
227 2020; Baby, Guillocheau, Boulogne, et al., 2018; Baby, Guillocheau, Morin, et al., 2018;
228 Guillocheau et al., 2012). The Orange River presently drains most of the southern African
229 Plateau, such that much of the sediment removed from the landscape is deposited in the Orange
230 River Basin. There is also fairly limited on-shore sediment storage in the Orange River drainage,
231 with no large continental basins, making this a good location for source to sink studies. The
232 sedimentary sequence in the Orange Basin basin records two periods characterized by high
233 sedimentary volumes and accumulation rates in Early and Late Cretaceous times, with
234 particularly high depositional volumes in the Orange Basin between 93.5 and 81 Ma (Baby,
235 Guillocheau, Morin, et al., 2018). The interval between 130 and 100 Ma as well as the Cenozoic
236 period are characterized by low sediment volumes and accumulation rates, though there is a
237 slight uptick in rates in the southern part of the margin since 11 Ma (Fig. 2, Baby, Guillocheau,
238 Morin, et al., 2018; Guillocheau et al., 2012). The basins off the southern and eastern coasts
239 show much lower volumes of sediment but with a similar pattern: high accumulation rates in the
240 Early and Late Cretaceous, followed by much lower sediment volumes in the Cenozoic (Fig. 2,
241 Baby, Guillocheau, Boulogne, et al., 2018; Braun et al., 2014; Tinker et al., 2008a). Together
242 these observations suggest intervals of increased erosion and sediment transport to the basins
243 surrounding southern Africa in the Early Cretaceous just following rifting and in the Late
244 Cretaceous ~100-65 Ma, with increased sedimentation rates first appearing in the Orange River
245 Basin ~95-90 Ma.

246 The sedimentary record of both the Indian (Baby, Guillocheau, Boulogne, et al., 2018)
247 and Atlantic (Baby, Guillocheau, Morin, et al., 2018) Margins show evidence for two phases
248 uplift at around 93-70 Ma and 25-15 Ma. Evidence comes from margin tilting and truncation,
249 forced regressive wedges recording a relative sea level fall with an amplitude higher than
250 100m/Ma and incised valleys (see Baby, Guillocheau, Boulogne, et al., 2018 for a discussion).
251 The stratigraphic record (Braun et al., 2014; Baby, Guillocheau, Boulogne, et al., 2018; Baby,

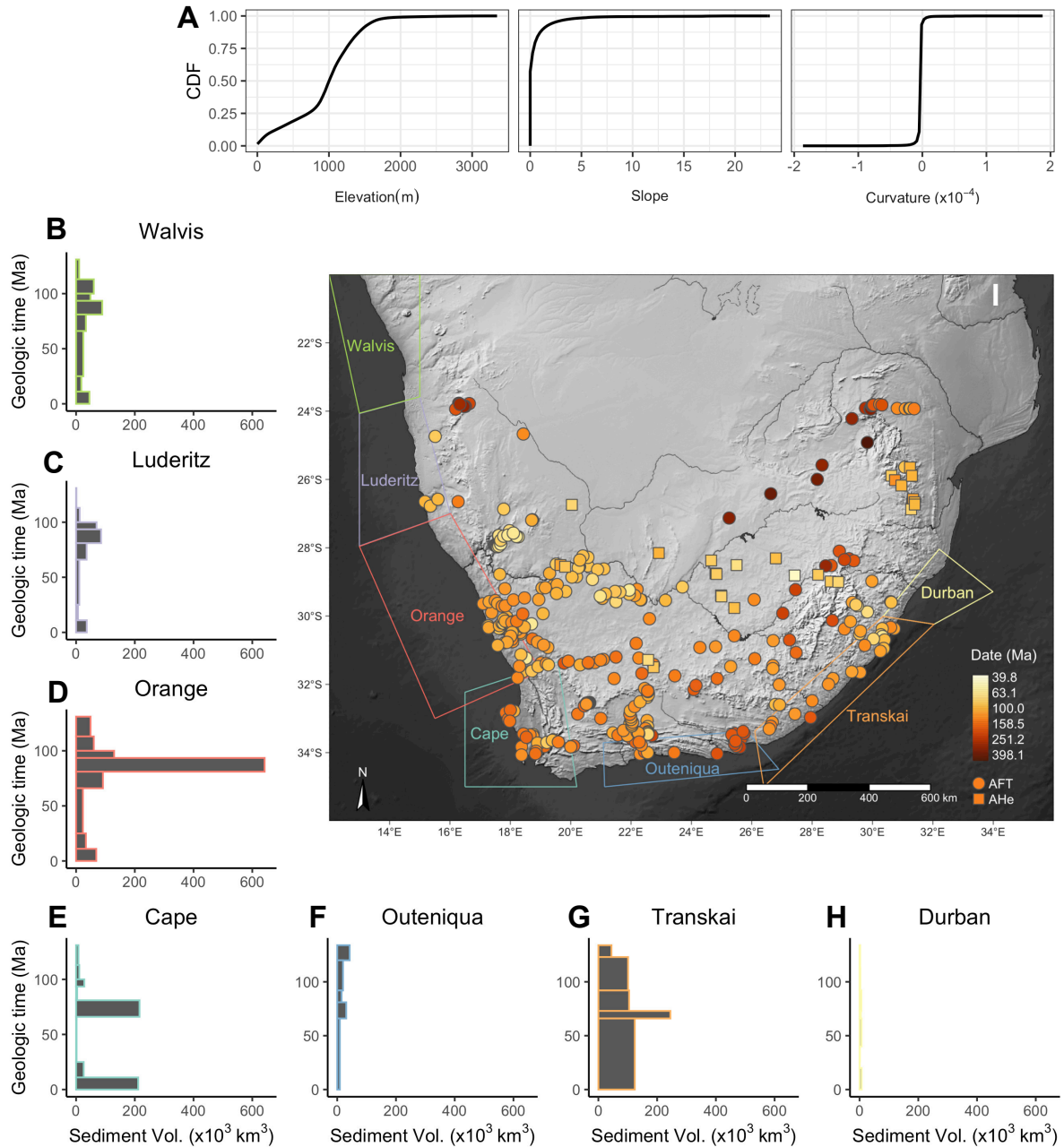


Figure 2. Data included in inversion modeling. A) Cumulative density functions (CDF) for present day elevation, slope, and curvature from southern Africa derived from the ETOPO1 dataset (Amante & Eakins, 2009). B-H) Sediment volumes deposited over time in the marine basins surrounding southern Africa (Baby et al., 2020). I) Shaded relief map showing the locations of low temperature thermochronology dates with color denoting age (Brown, 1990; Brown et al., 2002, 2014; De Wit, 1988; Flowers & Schone, 2010; Green et al., 2017; Kounov et al., 2009, 2013; Raab et al., 2002; Stanley et al., 2013; 2015; Stanley & Flowers, 2020; Tinker et al., 2008; Wildman et al., 2015, 2016, 2017)

253 Guillocheau, Morin, et al., 2018) indicates margin uplift and tilting of the Southern African
254 Plateau, starting to the east (Maputaland to Durban Margin) at 93 Ma and ending to the west
255 (Orange to Olifant Margin) at 81-70 Ma. After a period of no deformation (70-35 Ma),
256 significant uplift started again along the Durban to Maputaland Margin (25-15 Ma) and earlier
257 (35 Ma) along the Zambezi Margin (Ponte et al. , 2019).

258

259 2.2.2 Onshore constraints from thermochronology

260 Apatite fission-track (AFT) and (U-Th)/He (AHe) thermochronology are dating
261 techniques that track the cooling and heating of rocks through the upper ~1-6 km of crust and
262 can be used to constrain the long term burial and erosion of a region. AHe is sensitive to
263 temperatures of ~30-90°C (Farley, 2000; Flowers et al., 2009; Shuster et al., 2006). Assuming a
264 typical cratonic geothermal gradient of 20°C/km, AHe can be used to detect erosion in the upper
265 ~0.5-3.5 km of crust. AFT is sensitive to somewhat higher temperatures of ~60-110°C (Green et
266 al., 1986) or ~2-4.5 km depth assuming the same cratonic gradient. Many studies have used low
267 temperature thermochronology to constrain the long-term erosion histories in southern Africa.

268 The majority of studies have used AFT on the high relief eastern (Brown et al., 2002),
269 southern (Green et al., 2017; Tinker et al., 2008b) and western (Gallagher & Brown, 1999b;
270 Kounov et al., 2009, 2013; Wildman et al., 2015, 2016) passive margins of the plateau (Fig 2).
271 These studies show two periods of accelerated erosion in the Cretaceous, the first at ~150-120
272 Ma following continental breakup and the second at ~100-70 Ma. This work also suggests
273 limited Cenozoic erosion, though Green et al. (2017) suggest an episode of burial and erosion of
274 parts of the Southwest Cape during the Cenozoic. AHe data across the eastern plateau
275 escarpment also detects a cooling phase at ~100 Ma and limits Cenozoic erosion to <750 m
276 (Flowers & Schoene, 2010). AHe data across the interior of the plateau record greater spatial
277 variability than the plateau edges. In the Proterozoic basement of the southwestern plateau AHe
278 data indicate an intensified erosion phase from ~110-90 Ma, whereas in the Archean basement of
279 the central plateau a wave of erosion migrated eastward from ~120 Ma to <60 Ma (Stanley et al.,
280 2013, 2015; Stanley & Flowers, 2020)[Stanley et al., 2013, 2015, 2020], and the central part of
281 the Kaapvall Craton shows limited erosion since before the breakup of Gondwana (Wildman et
282 al., 2017). These results also suggest limited Cenozoic erosion of ~1 km or less.

283 Cosmogenic nuclide derived erosion rates suggest that erosion rates on both the plateau
284 surface and the coastal plain have been slow over the last few Myr. Most erosion rates, both
285 catchment averaged and bedrock, are <10 m/Myr (Bierman et al., 2014; Chadwick et al., 2013;
286 Cockburn et al., 1999, 2000; Decker et al., 2013; Dirks et al., 2016; Fleming et al., 1999; Kounov
287 et al., 2007; Makhubela et al., 2019; Scharf et al., 2013), one to two orders of magnitude lower
288 than thermochronologically derived rates for the Cretaceous. However, several studies focused
289 around river channels suggested slightly higher denudation rates (12 to 255 m/Ma) highlighting
290 some potential landscape variability (Erlanger et al., 2012; Keen-Zebert et al., 2016).

291

292 2.2.3 Onshore constraints from geological observations

293 Early geomorphologists described and correlated a number of geomorphic surfaces across
294 the southern African landscape that were attributed to cycles of uplift and denudation (e.g.,
295 Dixey, 1955; King, 1942, 1950; Partridge & Maud, 1987). Age assumptions for these surfaces
296 suggest plateau uplift in the Cenozoic (Burke, 1996; Burke & Gunnell, 2008; Partridge & Maud,
297 1987), but arguments used for dating are quite poor and the uplift scenario is questionable.
298 Recent work suggests that the surfaces in the plateau interior are mid to Late Cretaceous in age
299 based on cross cutting kimberlites (Baby, 2017). Pediments and wave cut platforms on the
300 continental margins are thought to be younger (<25 Ma, Baby, 2017). In the lower Orange River
301 Valley, these surfaces and alluvial terraces were used to argue for >200 m of uplift of this region
302 in the Cenozoic (Dauteuil et al., 2015).

303 Reconstructed thicknesses of the Karoo Basin can help constrain total erosion magnitudes
304 since ~180 Ma. The amount of material denuded across the main Karoo basin on the plateau
305 surface is estimated at ~0.5-3 km of material (Hanson et al., 2009), but vary based on location,
306 reconstruction method, and the proposed thinning rates for the units (Hanson et al., 2009;
307 Hawthorne, 1975; Johnson et al., 1996). Similar efforts at reconstructing stratigraphic
308 thicknesses on the southern margin suggest a range of erosional magnitudes from 4-11 km, in
309 line with AFT data (Richardson et al., 2017). Kimberlites can contain crustal xenoliths that
310 record the sedimentary cover present at the time of eruption and provide additional information
311 on erosional timing. Upper crustal xenoliths from kimberlites suggest that the Karoo sedimentary
312 section in the central plateau was removed in the Cretaceous in a west to east pattern that is
313 consistent with the AHe data (Hanson et al., 2009; Stanley et al., 2015). In addition, crater lake

314 sediments preserved in the ~75-65 Ma kimberlite pipes in the western Plateau suggest that this
315 area has seen very limited erosion since that time (A. Moore & Verwoerd, 1985; Scholtz, 1985;
316 Smith, 1986).

317

318 **3. Modelling methods**

319 3.1 Modelling strategy and data

320 We seek to test the three proposed intervals for the rise of the southern African plateau
321 using the breadth of erosion and sedimentation data that is now available here. To do this we use
322 a large-scale landscape evolution model to predict thermochronology dates, sediment fluxes, and
323 topography from different uplift inputs. We explore which parameter sets fit the observations
324 best using inversion methods combined with an optimization algorithm. The parameter space is
325 too large to sample in its entirety, so we use the neighborhood algorithm (NA, for full description
326 see Sambridge, 1999), to guide a total of 300,000 model runs varying 11 parameters (Table 2).
327 We then compare model results to three different types of observations: thermochronology dates,
328 marine sediment flux volumes, and topographic metrics.

329 The thermochronology data include 363 published AFT dates from Precambrian
330 basement and Karoo sedimentary rocks (Belton & Raab, 2010; Brown et al., 1990, 2002, 2014;
331 Green et al., 2017; Kounov et al., 2009, 2013; Raab et al., 2002; Tinker et al., 2008b; Wildman et
332 al., 2015, 2016, 2017) and 29 average AHe dates from Precambrian basement and Cretaceous
333 kimberlites and mafic rock samples (Flowers & Schoene, 2010; Stanley et al., 2013, 2015;
334 Stanley & Flowers, 2020). The full data table can be found in the supplementary materials Table
335 S1. Samples span from across southern Africa between 23.5°S and 36°S and cover both the
336 coastal margins and the plateau interior, though there is more data from the coastal regions (Fig
337 2).

338 The sediment flux data comes from volume estimates in seven marine basins on the
339 western and southern coasts of southern Africa (Fig 2). These volumes were calculated from
340 seismic constraints and borehole observations (Baby et al., 2020; Baby, Guillocheau, Boulogne,
341 et al., 2018; Baby, Guillocheau, Morin, et al., 2018). They are estimates of the terrestrially
342 derived sediment and have been corrected for in-situ carbonate production, porosity, and
343 compaction. Tables of the sedimentary volumes and basins are located in the supplement (Table
344 S2).

345 The present-day topography is derived from the ETOPO1 one arc minute global
346 topographic and bathymetric dataset (Amante & Eakins, 2009). Topography ranges from sea
347 level to 3376 m elevation, with a median elevation of 1037 m (Fig 2).

348

349 3.2 Forward model setup

350 3.2.1 Model setup and uplift

351 The landscape model runs from 145 Ma to present with timesteps of 1 Myr.
352 Parameterization of the model allows for topographic development corresponding to the three
353 main phases that have been proposed for uplift of the Kalahari Plateau: 1) Initial topography that
354 represents topography formed prior to Gondwana breakup, 2) A phase of uplift and continental
355 tilting in the Cretaceous, and 3) A phase of block uplift in the Cenozoic (Figure 3, Table 1). The
356 magnitude and time of uplift during these phases are variable within the inversion (Table 2).

357 The initial topography is the first phase of uplift input, representing any plateau
358 development that occurred prior to or during Gondwana breakup. All models start with 5% of
359 today's topography (0-150 m) to seed the drainage basins. This is then uplifted uniformly within
360 the first timestep by an additional plateau height h_0 which induces a flexural response at the
361 margins, mimicking rifted margin topography (Figure 3, Table 2). We seed the drainage basins
362 to reflect the current basins because the geologic record indicates that large, west-draining river
363 systems have been persistent in southern Africa since Gondwana breakup (e.g., M. C. J. de Wit,
364 1999). This westward draining nature of the plateau is important for determining where sediment
365 is routed, and we found that such a drainage geometry was difficult to create spontaneously. 5%
366 of today's topography is sufficient to setup a west draining geometry, but low enough magnitude
367 that it can be easily disrupted by uplift imposed later in the model.

368 In the Cretaceous we impose a phase of continental tilting that initiates in the east at a
369 time t_{init} . It tilts linearly to the west, reaching a maximum height of h_{tilt} 5 Myr after uplift initiates
370 (Fig 3, Table 2). The continent remains tilted for a duration of time t_{tilt} , at which point uplift
371 begins from the west reaching the same height and a flat uplift after 5 Myr (Fig 3). The continent
372 then retains this dynamic uplift for the rest of the model run. We chose this continental tilting
373 shape for the Cretaceous uplift phase because previous modeling (Braun et al., 2014) showed
374 that this was important for producing the large pulse of sediment observed in the basins off the
375 west coast. Additionally, we found that the tilting geometry was best for preserving a large-west

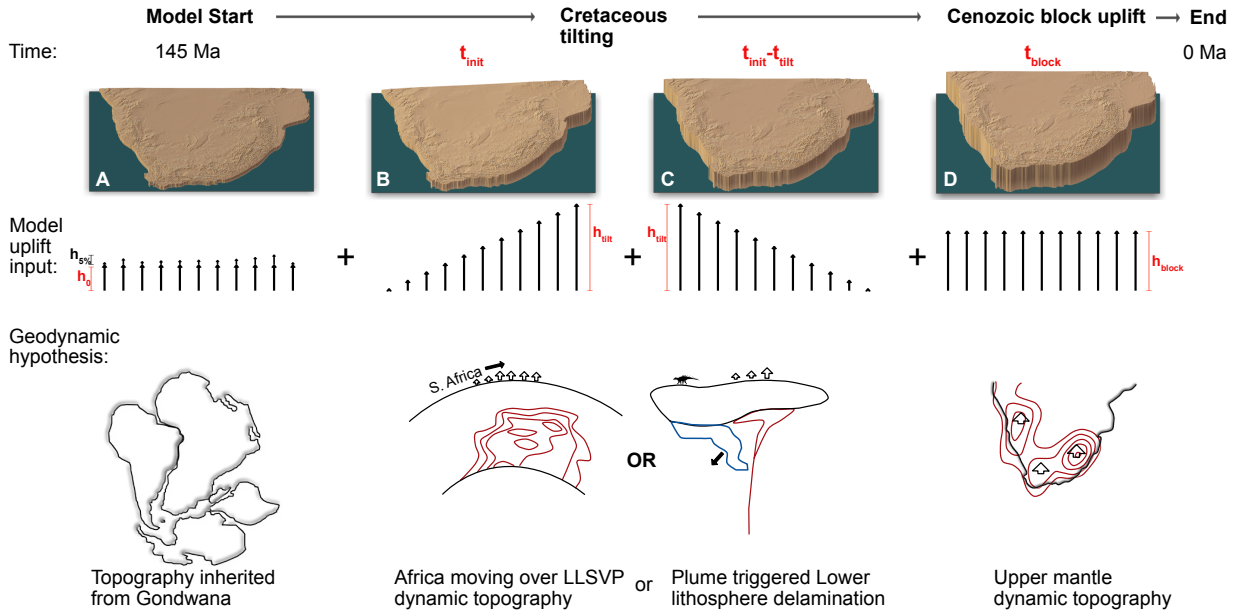


Figure 3. Schematic diagram of uplift imposed on the model through time. Parameters in red are variable in the inversion, while black are fixed. During the first time step (A), an uplift of height h_0 plus 5% of present day topography is imposed. At time t_{init} (B) a linear tilt is imposed as a vertical stress at the base of the model, and after t_{tilt} an opposing tilt to flatten the continent is imposed (C). Finally, at t_{block} a vertical stress at the base of the model is imposed to create an additional height of h_{block} (D). It should be noted that uplifts that are imposed as a vertical stress may produce magnitudes of rock uplift and erosion higher than the uplift amount due to isostatic feedback. Times are shown in geologic time. Bottom panels show cartoons depicting geodynamic hypotheses being tested at each stage. Uplift at model start represents topography inherited from prior to Gondwana breakup. Cretaceous tilting could be due to movement of Africa over a dynamic topography high due to the lower mantle LLSVP or lower lithosphere delamination triggered by kimberlite magmatism. Cenozoic uplift could be due to upper mantle buoyancy, perhaps denoted by present day free air gravity anomaly highs (after Winterbourne et al., 2009). See Table 1 for more explanation.

377 draining drainage basin geometry while many other uplift shapes we tested disrupted this
378 drainage network.

379 Finally, in the Cenozoic, at a time t_{block} , a phase of dynamic block/uniform uplift is
380 imposed with a magnitude h_{block} (Fig 3, Table 2). Once its maximum value is reached, the uplift
381 is maintained until the end of the model run.

382 The model domain ranges from 20°S to 35°S and 12°W to 36°W and is discretized on a 1
383 arc-second grid. For simplicity, base level remains fixed at the present-day coastlines throughout
384 the model run, and the northern boundary is a reflective, no-flux boundary. The model starts with
385 a uniform, 2 km thick softer layer representing the Karoo basin sediments and basalts overlying a
386 harder layer representing the Precambrian basement.

Variable Parameter	Units	Value Range	Hybrid best fit	Cretaceous best fit
K_r : Erosivity	$m^{0.2}/yr$	10^{-7} to 10^{-4}	3.387×10^{-6}	7.545×10^{-5}
ε_c : Threshold for erosion	m/yr	10^{-5} to 10^{-2}	1.111×10^{-4}	9.544×10^{-3}
T_{max} : Temperature at base of 120 km thick model lithosphere	°C	2400 to 5000	4430	4987
R_k : Ratio of thermal diffusivity between 2km thick Karoo sedimentary cover and underlying basement		0.3 to 1	0.307	0.310
R_D : Ratio between volume of material eroded and volume of material deposited in the marine basins		1 to 5	3.625	3.005
h_0 : height of initial base plateau in first time step	m	200 to 2000	233.2	206.1
t_{init} : Geologic time when uplift and tilting initiates in the east	Ma	120 to 75	94.72	97.50
h_{tilt} : Magnitude of Cretaceous tilting	m	200 to 3000	481.8	1414.5
t_{tilt} : Duration of time continent remains tilted before uplift initiates in the west	Myr	5 to 35	21.86	5.905
t_{block} : Geologic time of second phase of block uplift	Ma	40 to 0	33.09	22.19
h_{block} : amount: magnitude of second phase of uplift	m	0 to 2000	824.2	0.731

387 Table 2A – Variable parameters in inversion model, their ranges, and their values from the best fit models
388 from the Cretaceous and Hybrid Scenarios
389
390
391
392
393

Fixed Parameter	Units	Value	Justification
n : Slope exponent in stream power law		1	Literature values range from 0 to 4, $n=1$ chosen for numerical efficiency
m : Drainage area exponent in stream power law		0.4	Literature values range from 0 to 2, ratio of m/n derived from slope-area relationships in natural landscapes ranges from 0.35-0.6 (Kirby & Whipple, 2012; Whipple, 2004; Whipple & Tucker, 1999)
T_e : Elastic thickness	km	20	Effective elastic thickness estimates for southern Africa range from ~10 km near the coasts to >70km in the cratonic interior (Doucouré et al., 1996; Pérez-Gussinyé et al., 2009). We have chosen a value representative of the continental margins because flexural effects are most important to the landscape there.
t_{up} : time period over which each dynamic uplift stage is imposed	Myr	5	It is geologically unreasonable for uplift to occur instantaneously
Karoo layer thickness	km	2	Soft layer representing sediments and basalt overlying basement that can also have different thermal diffusivity.
Karoo layer erosivity	$m^{0.2}/yr$	$30(K_f)$	Braun et al. (2014) demonstrated that a soft layer was important for reproducing the Cretaceous sediment pulse
E : Young's modulus	GPa	1×10^{11}	
ν : Poisson's ratio		0.25	
ρ_c : crustal density	kg/m^3	2750	
ρ_a : asthenospheric density	kg/m^3	3300	
κ : thermal diffusivity of basement	m^2/yr	25	
Lithospheric thickness	km	120	
Kinetic model for apatite fission track annealing			Crowley et al. (1991)
Kinetic model for He diffusion in apatite			Farley (2000)

394 Table 2B – Fixed parameter values and justification.

395

396 3.2.2 The landscape evolution model

397 The landscape evolution model solves the basic stream power model for bedrock river
398 incision (Howard & Kerby, 1983),

399

$$\frac{\partial h}{\partial t} = U - \max(0, K_f S^n A^m - \varepsilon_c) \quad (1)$$

400 where h is the height of the topography, t is time, U is uplift rate, S is slope, A is drainage area, K_f
 401 is the erosion efficiency scaling parameter, m and n are constants, and ε_c is an erosion threshold.
 402 Equation (1) is solved by the FastScape algorithm (Braun & Willett, 2013). FastScape is a very
 403 efficient, first order, implicit, finite difference algorithm for solving the stream power equation
 404 that makes it possible to run many forward models rapidly enough to complete inversions. The
 405 values of K_f , m , and n are not well constrained but depend dominantly on climate, lithology, and
 406 hydrology. We use standard values of $n=1$ and $m=0.4$ and allow K_f to vary over several orders of
 407 magnitude between 10^{-7} and $10^{-4} \text{ m}^{0.2}/\text{yr}$. The top 2 km of the model is a layer of soft material
 408 representing the Karoo basin where K_f for the layer is 30 times the value of K_f for the underlying
 409 material. All parameter values and their justification can be found in Table 2 (see Croissant &
 410 Braun, 2014, for a more thorough discussion of the values of the erosional parameters). The
 411 introduction of the erosion threshold, ε_c with units of m/yr, implies that some base level of
 412 stream power is needed to erode the landscape. ε_c is also allowed to vary over several orders of
 413 magnitude (Table 2). Flow is routed using a D8 grid connectivity, and local depressions are filled
 414 using the algorithm of Cordonnier et al. (2019). We do not include a model for hillslope
 415 processes because they cannot be adequately represented at the scale of our model (i.e., grid
 416 resolution of 1x1 km). This is a highly simplified description of erosion, and unlikely to capture
 417 the true complexity of erosion processes across the southern African landscape. However we feel
 418 it is sufficient for comparison at the scale of our model and data types we have incorporated.

419 We compute the flux of sediment leaving the continent along various sections of the
 420 continental margin corresponding to major depocenters as shown in Figure 2. We introduce a
 421 deposition ratio, R_D , which multiplies the eroded flux to produce a depositional flux into the
 422 marginal basins that is compared to observed fluxes. This ratio accounts for imbalances in the
 423 amount of material eroded and deposited that could be caused by processes such as chemical
 424 denudation or transport of material away from the depocenter.

425 The LEM is coupled to an isostatic model that includes flexure of a thin elastic plate:

$$D \frac{\partial^4 U}{\partial x^4} + D \frac{\partial^4 U}{\partial y^4} + D \frac{\partial^4 U}{\partial x^2 \partial y^2} = \Delta \rho g U + \rho_c g \Delta h + \sigma_{DT} \quad (2)$$

426 where D is the flexural rigidity, ρ_c is the crustal density, $\Delta\rho$ is the density difference between ρ_c
 427 and the asthenospheric density, and σ_{DT} is an imposed basal stress that could represent viscous
 428 stress from mantle flow or an isostatic response from delamination of the lithospheric mantle. D
 429 is related to Young's modulus (E), the elastic thickness (T_e) and Poisson's ratio (ν):

430

$$D = \frac{ET_e^3}{12(1 - \nu^2)} \quad (3)$$

431 The flexure equation is solved using the Fast Fourier Transform method in the spectral domain
 432 on a fixed grid using methods similar to Nunn and Aires (1988).

433 Uplift is imposed as a vertical stress field along the base of the lithosphere through the
 434 flexural-isostatic model (equation 2) as σ_{DT} , where σ_{DT} is the stress required to lift the surface
 435 topography to the imposed height. In this setup, surface erosion results in the rebound of surface
 436 topography such that the weight of the surface topography remains equal to the basal load. This
 437 can continue until the deflection at the base of the crust is sufficient to balance the load.

438

439 3.2.3 Thermal Model

440 A 1D thermal model is coupled to the landscape model to predict cooling dates from the
 441 modeled erosion history for comparison with the observed data. For each location where a
 442 predicted cooling date is needed, the erosion rate is stored for each time step and used to generate
 443 an exhumation history at the end of the model run. These erosion rates are then used to solve the
 444 1D heat equation:

445

$$\frac{\partial T}{\partial t} + \dot{E} \frac{\partial T}{\partial z} = \kappa \frac{\partial^2 T}{\partial z^2} + \frac{H}{c} \quad (4)$$

446 where c is the heat capacity, \dot{E} is the erosion rate, κ is the thermal diffusivity, and H is the heat
 447 production by radiogenic elements. The implementation in the model also allows for layers with
 448 differing thermal diffusivities, and their thicknesses are adjusted throughout the model run to
 449 account for their erosion. The solution is used to compute time-temperature paths and predict
 450 dates for thermochronological systems (Braun et al., 2006).

451 The top and base of the models at fixed temperatures, with the surface at 15°C and T_{max} at
 452 the base of a 120 km thick lithosphere which correspond to surface geothermal gradients

453 between ~ 20 and $42^\circ\text{C}/\text{km}$. The thermal diffusivity of the soft layer at the top of the model
454 representing the Karoo sedimentary sequence can vary as a ratio of the basement thermal
455 diffusivity, R_K , allowing for a thermal blanketing effect of up to 3 times (Table 2).

456

457 3.3 Inversion methods

458 We use the NA optimization (Sambridge, 1999) to guide the sampling of the large
459 parameter space. At the start of the inversion, 10,000 random sets of parameters are selected
460 from within the specified ranges (Table 2), and a forward model is run with each parameter. For
461 each model, a misfit that measures how well the predicted values match the observed values is
462 calculated. For each subsequent iteration of 1000 runs, the NA preferentially samples from areas
463 of the parameter space with lower misfit values, while still casting a wide net (see Sambridge,
464 1999, for details).

465 The construction of a misfit function that can assign a single numerical value of how well
466 each forward model fits the observations is central to the inversion method, however combining
467 assessments of different data types is nontrivial. We first compute an individual misfit for each
468 separate data type, and then we combine these into a single misfit value for the model run.

469 For the topographic metrics, the misfit is calculated by comparing the distributions of the
470 predicted and observed topography using the two sample Kolmogorov–Smirnov (KS) statistic.
471 We compare the distributions of present-day topographic height, slope, and curvature with those
472 from our model results. We use cumulative distribution functions (CDFs) for each of these
473 metrics calculated at the same spatial scale as the model resolution. We compare CDFs rather
474 than directly comparing the topography because it is unlikely that the model will replicate
475 specific features of the model (such as exact locations of valleys and mountain tops) but should
476 be able to replicate broader characteristics of the topography. The KS statistic measures the
477 distance between the predicted and observed distribution, yielding a value between 0 (for
478 identical distributions) and 1 (for distributions that do not overlap). We calculate three individual
479 misfits, M_{height} , M_{slope} , and M_{curve} that are the KS statistic for the comparison between the
480 predicted and observed topographic height, slope, and curvature distributions.

481 Terrigenous sediment flux volumes have been calculated for a number of time periods in
482 seven basins for a total of 50 volumes (Baby et al., 2020; Baby, Guillocheau, Boulogne, et al.,
483 2018; Baby, Guillocheau, Morin, et al., 2018; Figure 2, Table S2). If N is the total number of

484 volume calculations, the misfit for the flux, M_{flux} , takes the form of the square-root of the L₂-
 485 norm of the weighted difference between the predicted ($V_{i,pred}$) and observed ($V_{i,obs}$) volumes for
 486 the volume from each time period:

$$487 \quad M_{flux} = \frac{1}{N} \sqrt{\sum_{i=1}^N \frac{(V_{i,pred} - V_{i,obs})^2}{\sigma_{avg}^2}}$$

488
 489 where σ_{avg} is the average uncertainty across all the flux calculations ($13.7 \times 10^{12} \text{ m}^3$). M_{flux} can
 490 range from 0, for V_{pred} equal to V_{obs} , to very large when V_{pred} is very different from V_{obs} . Values
 491 of $M_{flux} < 1$ indicate that the predicted values match the observed values within the average
 492 uncertainty.

493 The misfit for the thermochronology data, M_{thermo} , takes a similar form to the flux misfit:

$$494 \quad M_{thermo} = \frac{1}{N} \sqrt{\sum_{i=1}^N \frac{(a_{i,pred} - a_{i,obs})^2}{\sigma_{i,obs}^2}}$$

495 where $a_{i,pred}$ is the predicted thermochronologic date for each location from the model run, $a_{i,obs}$
 496 is the observed thermochronologic date at that location, and $\sigma_{i,obs}$ is the uncertainty associated
 497 with that date. N is the total number of thermochronologic dates included in the model, in this
 498 case 392 (Fig 2; table S1). In most situations the cooling dates for low temperature
 499 thermochronometers are expected to vary systematically with elevation (e.g., Braun, 2002).
 500 Because we cannot expect the model to reproduce the exact characteristics of the landscape,
 501 $a_{i,pred}$ is taken from the location within a 20km radius that is closest in elevation to the observed
 502 date. M_{thermo} also ranges from 0 for an exact match between the predicted and observed dates to
 503 very large for a poor match with $M_{thermo} < 1$ indicating that the model predictions match the
 504 observations within uncertainty.

505 The total misfit, M , for the model run is the sum of the five individual misfits for the
 506 different data types:

$$507 \quad M = M_{height} + M_{slope} + M_{curve} + M_{flux} + M_{thermo}$$

508 The misfit used to guide the parameter search in the inversion is therefore a combination of how
 509 well the model fits the combination of data types. It should be noted that the form of the misfit
 510 and how the different misfit types are weighted has a strong effect on the inversion results.

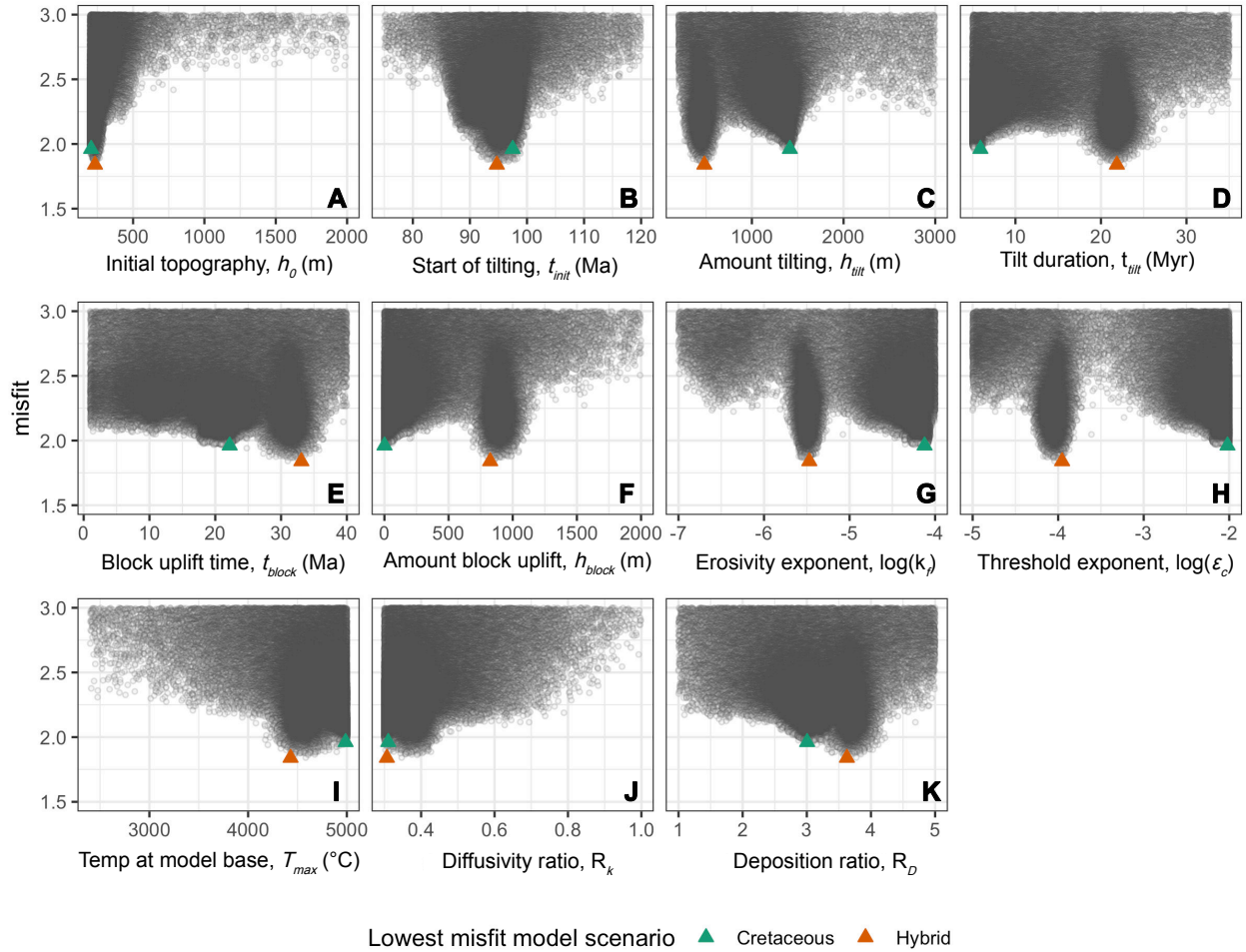


Figure 4: Plots showing the values of parameters for models with misfits < 3. Each grey circle represents one forward model and the value for a given parameter. The lowest points show the parameters converging toward value(s) with better fits to the data. Green and red-orange triangles show parameter values for best fit models from the Cretaceous and Hybrid Scenarios.

512 4. Results

513 4.1 Inversion Results

514 Results from topographic uplift driven inversions converge on two low-misfit parameter
515 sets (Figure 4). Misfit values for individual forward model runs in the inversion range from 1.8
516 to >500, and these two clusters of low misfit solutions contain all of the model runs with misfit
517 values less than 2. All low misfit models have similar thermal parameter values, with
518 temperatures at the base of the 120 km thick lithosphere converging at >4000°C (Fig 4I),
519 suggesting static geothermal gradients of >33°C/km, with the Karoo basin layer acting as a
520 thermal blanket that is 2 to 3 times more insulating than the underlying basement (Fig 4J) leading
521 to an even higher geotherm in the top 2 km. Finally, all models converge towards a value of 0.25
522 to 0.3 for R_D which indicates that only 1/3 to 1/4 of the volume of material eroded off the surface
523 is deposited in the basin (Fig 4K).

524 The two parameter sets differ in the timing and magnitude of topographic uplift. Both
525 indicate low initial topographies with plateau elevations <500 m (Fig 4A). Also, all low misfit
526 models have some Cretaceous uplift initiating in the east between 100 and 90 Ma (Fig 4B). The
527 two families of low misfit models differ in the magnitude of Cretaceous and Cenozoic uplift (Fig
528 4C, 4D, 4E, 4F). Figure 5 shows the topographic uplift over time for all models run, colored by
529 misfit value. The lowest misfit models (yellow) clearly split into two uplift patterns. One group,
530 which we will refer to as the Cretaceous Scenario, has ~1400 m of uplift in the Cretaceous, with
531 dynamic tilting starting in the east, followed by uplift in the west that flattens the plateau after
532 <10 Myr of tilting. This Cretaceous Scenario has very low magnitudes of uplift in the second
533 Cenozoic block uplift phase, less than a few hundred meters, and the timing is not well
534 constrained. The other group of low misfit models we will refer to as the Hybrid Scenario. These
535 models have lower magnitudes of uplift during Cretaceous tilting, ~300-800 m initiating in the
536 east at a similar time as the Cretaceous Scenario, but remain tilted for longer, >20 Myr, so uplift
537 in the west occurs later (Fig 5). In the Hybrid Scenario, the majority of uplift occurs at ~35-25
538 Ma with > 800 m of Cenozoic block uplift. Both scenarios end with similar magnitudes of total
539 uplift throughout the model run, on the order of 1500-1800 m, leading to a clear tradeoff between
540 the amount of uplift in the Cenozoic and Cretaceous phases that is visible in a scatter plot of
541 these parameter values and misfits (Fig 6A). Snapshots of the topography through time for the
542 best fit models are shown in Figure 7 (also available as Movie S1 in the supporting information).

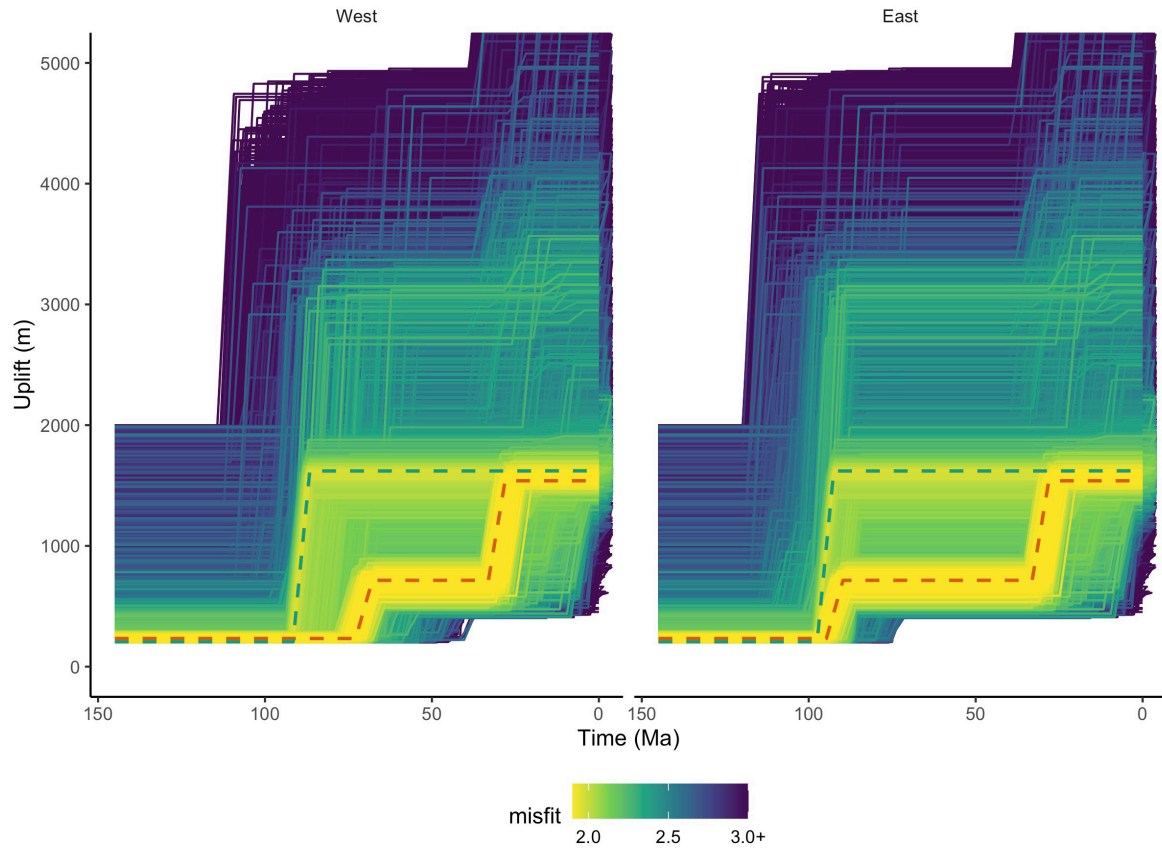


Figure 5. Uplift through time for the east edge (left panel) and west edge (right panel) of the model domain. Time is geologic time. Each line represents one forward model and is colored by the misfit value. Green dashed line is the best fit model for the Cretaceous Scenario and red-orange dashed line is the best fit model for the Hybrid Scenario.

543

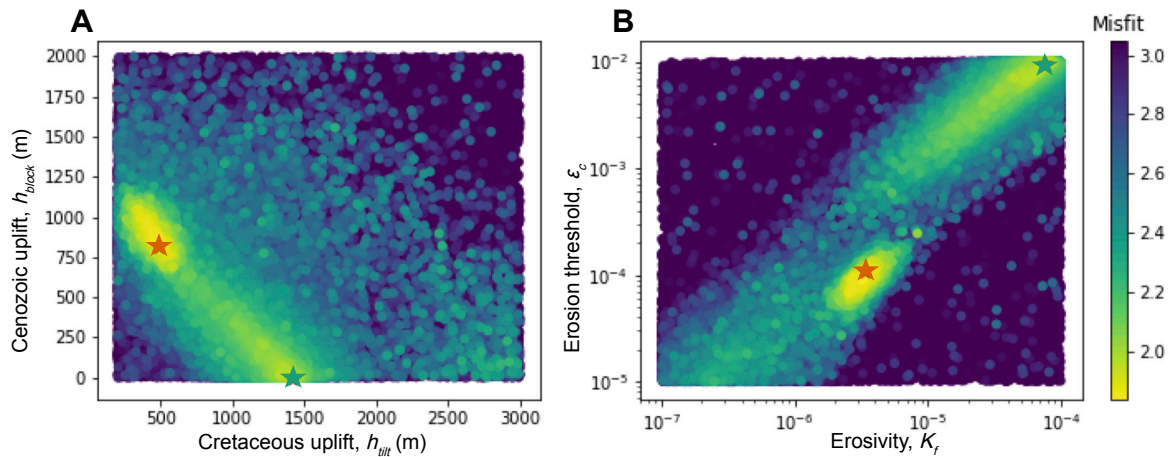


Figure 6. Scatter plots showing tradeoffs between parameter pairs. Each dot represents the parameter values for one forward model run and is colored by the misfit for the model. The low-misfit models show a tradeoff between the amount of Cenozoic uplift and the amount of Cretaceous uplift (A) as well as the erosion threshold and the erosivity (B). Green star shows the best fit model for the Cretaceous Scenario and red-orange star for the Hybrid Scenario. Many other combinations of model parameters are possible, but these two pairs show the strongest cross correlation.

544

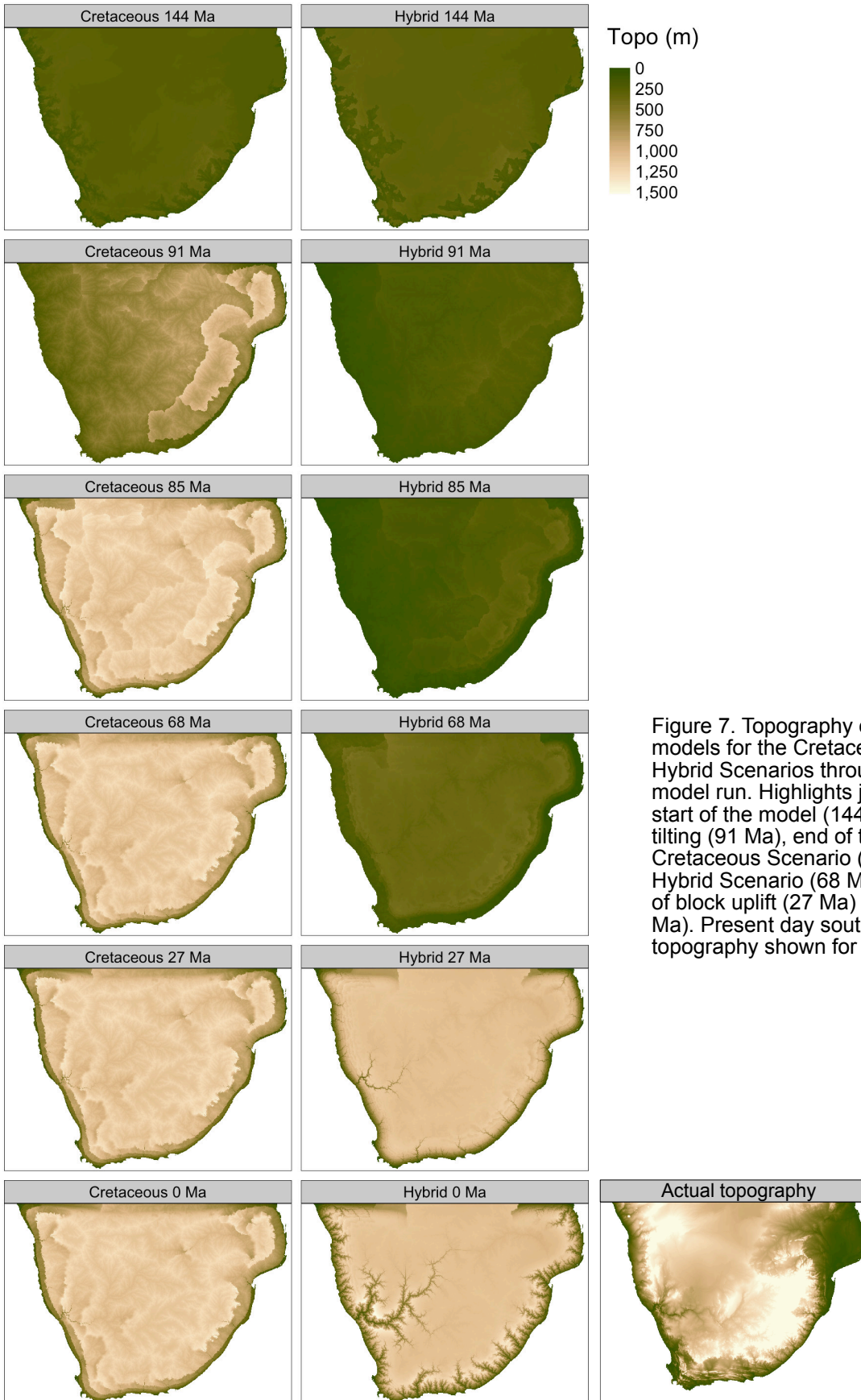


Figure 7. Topography of best fit models for the Cretaceous and Hybrid Scenarios through the model run. Highlights just after the start of the model (144 Ma), during tilting (91 Ma), end of tilting for Cretaceous Scenario (85 Ma) and Hybrid Scenario (68 Ma) and time of block uplift (27 Ma) to the end (0 Ma). Present day southern African topography shown for comparison.

546 The Cretaceous and Hybrid Scenarios differ most obviously in their uplift patterns, but
547 they also converge to different erosional parameters (Figs. 4G, 4H). The Cretaceous Scenario
548 converges towards values of the erosional parameter, K_f , between 2×10^{-4} and 6×10^{-4} $\text{m}^{0.2}/\text{yr}$ and
549 erosional threshold (ϵ_c) values of between 1×10^{-2} and 4×10^{-2} m/yr . The Hybrid Scenario
550 converges with values for K_f and ϵ_c over an order of magnitude lower, with K_f between 4×10^{-5}
551 and 9×10^{-5} $\text{m}^{0.2}/\text{yr}$ and ϵ_c values of between 9×10^{-3} and 5×10^{-4} m/yr . This means that the Hybrid
552 Scenario has relatively more durable material with K_f and a lower threshold for erosion as
553 compared with the Cretaceous Scenario. There is also an tradeoff between K_f and ϵ_c that is
554 visible in scatter plots of their parameter values and misfit (Fig 6B).

555

556 4.2 Data-Model comparison

557 The predictions from the lowest misfit model from the Cretaceous and Hybrid Scenarios
558 are compared with the observed data in Figures 8 and 9. Overall the two models have a similar
559 fit to the data. Both replicate the large pulse of sediment observed in the Orange River Basin in
560 the Cretaceous and the overall lower fluxes observed elsewhere (Fig 8). Neither model produces
561 the larger fluxes seen off the SW coast in the Cape Basin or in the Transkai Basin (Fig 8). Both
562 models fit the median of the elevation, slope, and curvature distributions (Fig 9). Neither model
563 produces the highest elevations, slopes, and curvatures observed in reality. The Hybrid Scenario
564 has a closer match to the shape of the elevation distribution, while the Cretaceous Scenario fits
565 the curvature distribution more directly. Neither model is able to reproduce the complexity
566 observed in the thermochronology data, but both do a reasonably good job at replicating the
567 average of the thermochronology dates, especially the AFT dates (Fig 9). The Cretaceous
568 Scenario predicts overall slightly younger dates, which is a slightly better fit to the AHe dates
569 especially. Overall, the models show fairly similar fits to the data and, while the models do not
570 reproduce some of the details and structure in the natural data, they are a good match to the
571 large-scale patterns observed.

572

573 5. Discussion

574 5.1 The role of data and the misfit function in identifying suitable models

575 A major and initially surprising take-away from the inversion results is that the existing
576 data cannot differentiate between two low misfit parameter sets, at least with the data we

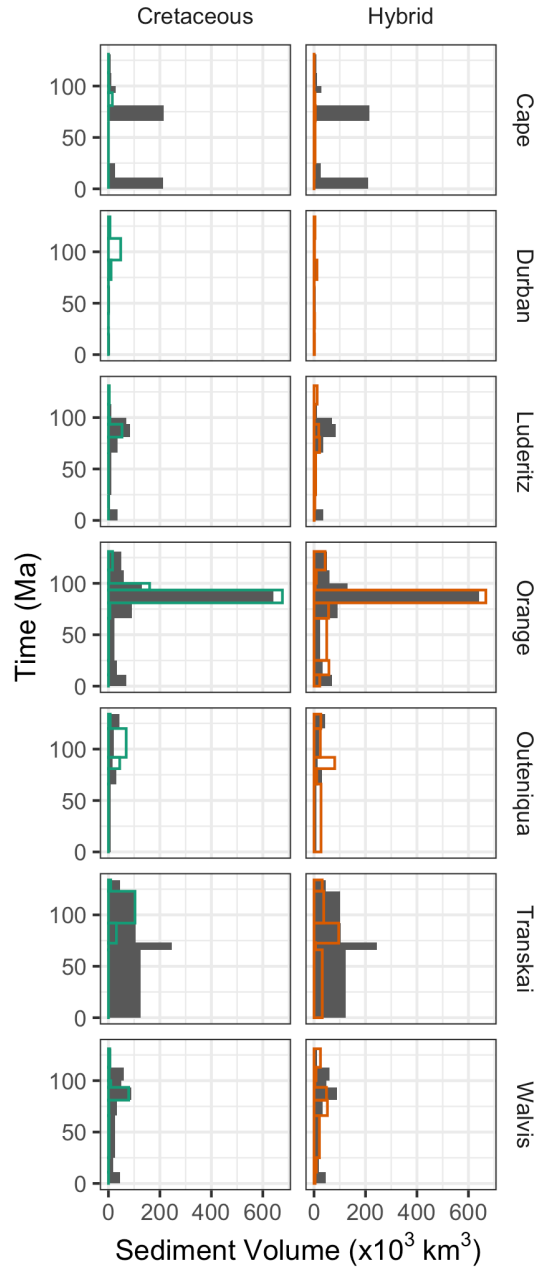


Figure 8. Sediment volumes through time from best fit models (colored outlines) compared with measured volumes from basins surrounding southern Africa (grey bars, Baby et al., 2020). See Fig 2 for locations of basins.

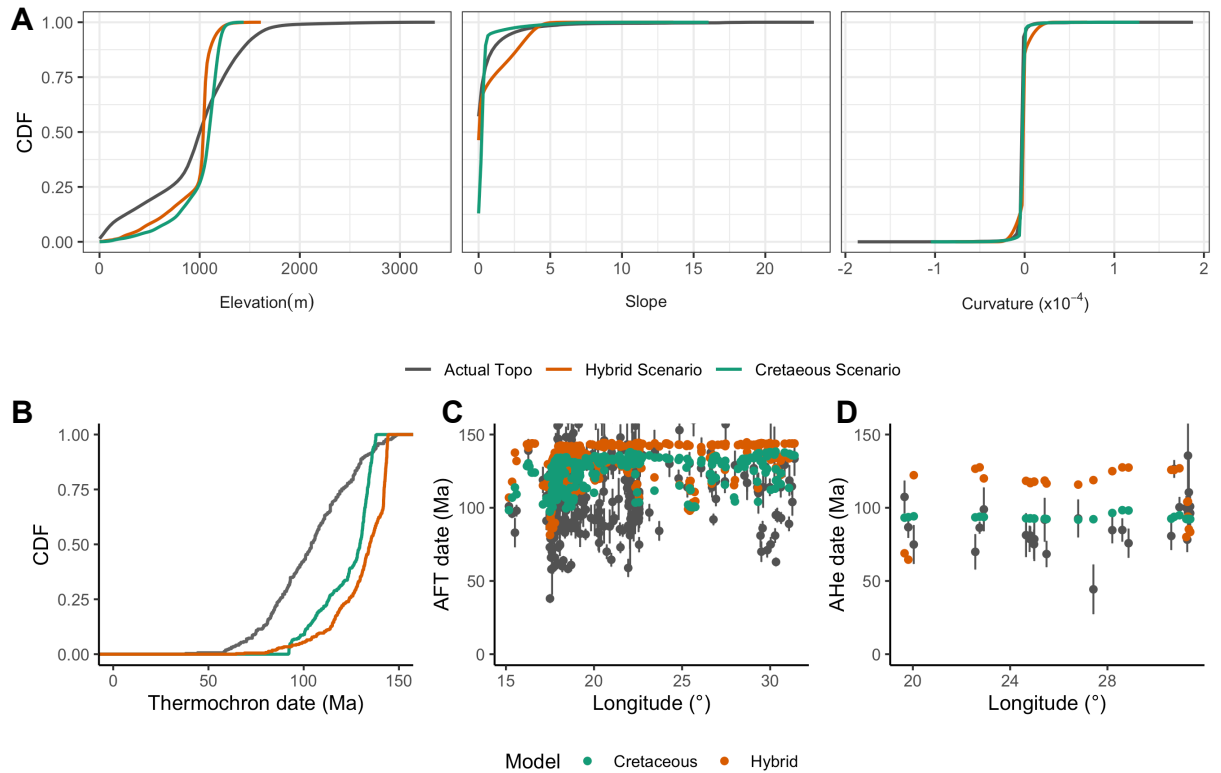


Figure 9. A) Comparison of CDFs of present day southern African topographic metrics (grey) to best fit model runs from the Cretaceous Scenario (green) and the Hybrid Scenario (red-orange). B) Comparison of the CDF for all thermochronology dates used in the inversion (AFT and AHe) between measured dates (grey) and modeled dates (colors). C) AFT dates plotted by longitude for observed data (grey) and modeled dates from the Cretaceous Scenario best fit (green) and Hybrid Scenario best fit (red-orange). D) same as in C but for AHe dates.

579 included and the current formulation of the misfit function. The uplift histories highlighted by
580 the model inversions broadly match with times when plateau development had previously been
581 proposed based on interpretation of the datasets that we have included (Table 1). We cannot
582 settle the timing of uplift debate based on our results at present, but we can provide some insight
583 into what is controlling the inversion results and what might allow future efforts to provide a
584 more definitive answer.

585 The results of the model run are highly sensitive to the data used, the uncertainties
586 associated, as well as the formulation of the misfit function and how those uncertainties are
587 incorporated into the misfit function. No model is able to reproduce the observed data perfectly,
588 and, given the simplifications made in the modelling exercise, we would not expect any model to
589 truly be able to reproduce the complexities in the data. However, we constructed the misfit
590 function to measure how well the model is able to capture the large scale trends in the data that
591 we see as most important: the major pulse of erosion and sedimentation observed in the
592 Cretaceous, low sedimentation and erosion rates observed in the Cenozoic, and plateau-like
593 topography with similar statistical characteristics to the current topography. We made choices in
594 constructing a misfit function that reflect our view of these as important aspects of the data.
595 However, different formulations of a misfit function are possible and would strongly affect the
596 inversion results. For example, there are many techniques that have been proposed for comparing
597 model outputs to topography (e.g., Barnhart et al., 2020; Howard & Tierney, 2012; Ibbitt et al.,
598 1999; Skinner et al., 2018) that range from direct pixel comparisons which retain the spatial
599 information to wholly aggregated statistical comparisons. We have chosen to compare statistical
600 distributions using the KS statistic because this is an appropriate measure of the broad
601 similarities between the topographies, but if it was decided that specific topographic features
602 were key to reproduce, a different metric might be more appropriate and it could change the
603 outcome of the inversion.

604 Similarly, combining the metrics from different data types requires some challenging
605 decisions about whether and how to weight the different data types that can potentially influence
606 the inversion outcome. We have chosen not to weight the different misfits, and just sum them as
607 the simplest solution. However, because the flux and thermochronology misfits take the form of
608 least-squares differences and can range from 0 to large, while topographic misfits can only
609 range from 0 to 1, the combined misfit is more sensitive to the thermochronology and flux

610 misfits even though we do not directly weight them. We feel that this is appropriate and that our
611 inversion yields model results that fit all data types adequately compared with the several other
612 misfit formulations that we tested. However, it should be noted that other choices about
613 weighting of the different data types could be made, and these choices could substantially affect
614 the inversion results.

615 Finally, the data included for comparison with model results strongly affects the
616 inversion, and the inclusion of additional data has the potential to differentiate between these
617 model scenarios. In fact, the results presented here can be used to guide future data collection
618 efforts and highlight what additional information would be most useful in constraining the uplift
619 histories of southern Africa. For example, the best fit models predict very different erosion rates
620 in the final 1 Myr timestep (Figure 10), with the Hybrid Scenario predicting higher erosion rates
621 focused along the main river network in canyons while the Cretaceous Scenario predicts very
622 low erosion rates throughout the landscape. Cosmogenic radionuclide-based bedrock erosion
623 rates can be compared to these predictions or included in future modelling efforts. Published
624 cosmogenic radionuclide based erosion rates for southern Africa are mostly low (on the order of
625 10^{-6} m/Myr, Fig 10; Cockburn et al., 2000; Decker et al., 2013; Dirks et al., 2016; Erlanger et
626 al., 2012; Fleming et al., 1999; Kounov et al., 2007; Makhubela et al., 2019; Scharf et al., 2013)
627 but are generally not from within major river canyons, making it difficult to compare where the
628 two landscape models differ the most prominently. One study focused directly on river valleys
629 fairly high in the river systems near the drainage divide yields rates an order of magnitude
630 higher, indicating there might be some spatial variation (Keen-Zebert et al., 2016). However,
631 terraces in the lower Orange River suggest a maximum incision rate of 6 m/Ma post-17 Ma (M.
632 C. J. de Wit, 1999). Additional data is needed to differentiate the two landscape models, and
633 the predicted patterns for recent erosion can provide guidance for future sampling campaigns.

634 Other aspects that future modelling could include are more complete of stratigraphic
635 architecture rather than just sediment volumes, which might favor a post-Eocene phase of uplift
636 (Baby et al., 2020; Baby, Guillocheau, Boulogne, et al., 2018; Baby, Guillocheau, Morin, et al.,
637 2018). If future efforts were able to more precisely date the erosion surfaces and pediments, for
638 example by (U-Th)/He dating of goethite, these could be more directly incorporated. A more
639 nuanced, spatial comparison of the modelled and observed topography might capture some of the
640 more distinctive features of southern Africa, potentially helping to distinguish uplift histories.

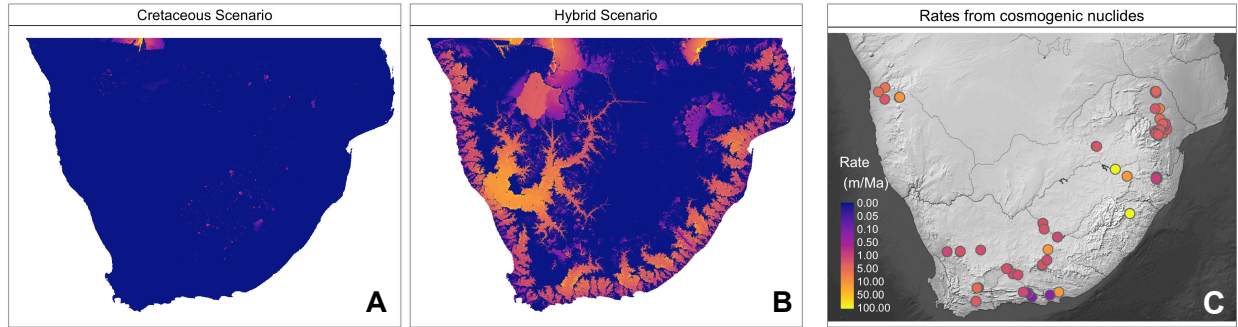


Figure 10. Predicted erosion rates for last 1 Myr timestep from each model (A, B) compared with recent erosion rates (over the last 0.1-2 Myr) derived from cosmogenic radionuclide studies (C). Data in C are published data from bedrock samples or river incision rates at particular locations (Kounov et al., 2007; 2015; Dirks et al., 2010; Cockburn et al., 2000; Erlanger et al., 2012; Glotzbach et al., 2016; Keen-Zebert et al., 2016; Bierman et al., 2014; Scharf et al., 2013; Decker et al., 2013)

642 5.2 Controls on erosional response to uplift

643 One of the challenges in elucidating paleotopography is how to quantitatively link
644 erosion rates or magnitudes derived from the rock record to changes in surface uplift or
645 topography. We make the assertion that we expect an erosional response to topographic uplift,
646 but the question is how much uplift is required to trigger erosion of a given magnitude, and what
647 might cause that to vary. By comparing to both topographic and erosional metrics in our
648 inversions, the results give us some insights into which parameters are most strongly controlling
649 the magnitude of erosion in response to the uplift we impose in the model, and what that might
650 mean for southern Africa's uplift history. We find that in this case, the ratio between the
651 erosivity coefficient, K_f , and our parameterization of an erosion threshold ϵ_c , plays an important
652 role in the magnitude and temporal span of erosion after an uplift event. We also find that the
653 shape of the uplift (tilting or block uplift) strongly effects the magnitude of erosion.

654 Braun et al. (2014) had already shown that continental tilting combined with a soft Karoo
655 layer overlying harder basement was key for producing a sediment pulse similar to the major
656 Cretaceous pulse in the Orange River Basin. Our results support that tilting is important and able
657 to produce a large erosion response by steepening the slopes across the interior of the continent.
658 Other shapes of uplift that we tried either disrupted the large, west draining Orange River
659 drainage network, did not reproduce the sediment pulse, or both. In addition to the tilting, we
660 found that adding a parameter representing a threshold for erosion was critical for reproducing
661 the pulse as well as the low sedimentation rates observed on the southern coast and throughout
662 the Cenozoic. Without this threshold, models would continue to erode substantially, especially
663 around the plateau margins even after the continent was no longer tilted. There is a clear
664 covariation between the threshold parameter, ϵ_c , and the erosivity, K_f , (Fig 6B) and parameter
665 sets outside this band were not able to create the observed sediment pulse.

666 The Cretaceous uplift phase in both low misfit scenarios is able to produce similar
667 magnitudes of erosion and sedimentation with very different magnitudes of uplift (Fig 11). The
668 parameters controlling the magnitude of erosion in response to a given uplift magnitude are K_f
669 and its ratio to ϵ_c , as well as the length of time the continent stays tilted. The Cretaceous Scenario
670 has higher magnitudes of uplift and tilting, ~ 1400 m, but for a shorter total time, on the order of
671 5 Myr. It also has a higher base erosivity, but also a relatively higher threshold ($\epsilon_c/K_f = 126$).
672 Higher magnitudes of uplift and tilting are needed for stream power to exceed the threshold, but

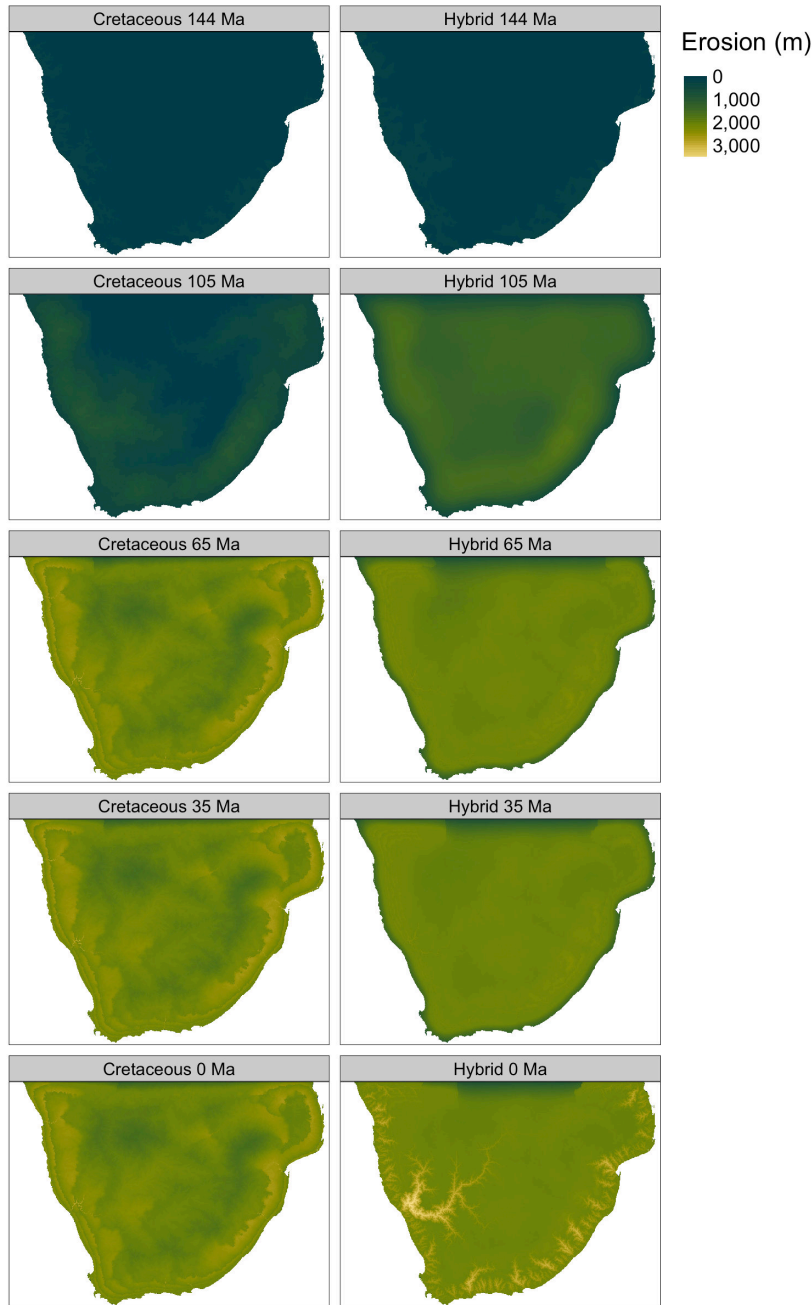


Figure 11. Erosion of the best fit models for the Cretaceous and Hybrid Scenarios throughout the model run. Highlights just after the start of the model (144 Ma), prior to Cretaceous tilting (105 Ma), after Cretaceous tilting (65 Ma), prior to Cenozoic block uplift (35 Ma) and after Cenozoic uplift at the end of the model run (0 Ma).

674 once exceeded, higher erosivity and steep slopes allow the model to erode relatively quickly. The
675 Hybrid Scenario, which only has ~500 m of uplift during Cretaceous tilting, has a lower
676 erosivity, but also a lower threshold with $\epsilon_c/K_f = 33$ for the best fit model. It also remains tilted
677 for longer, on the order of 20 Myr. This lower magnitude of tilt steepens slopes enough for
678 stream power to exceed the threshold, and the continent remains tilted long enough for
679 significant erosion to take place (Fig 11). The range in uplift magnitudes able to produce a
680 similar erosion response highlights the difficulty in inferring uplift directly from erosion records,
681 but also highlights the utility of landscape models, even fairly simple ones, to explore the range
682 of possibilities.

683 The low magnitude erosional response to widely varying Cenozoic uplift in the two
684 models further highlights the importance of the shape and style of uplift for how much erosion
685 occurs. One of the longstanding debates about southern African topography is how much of the
686 topography is “recent” which we define here as Cenozoic. The debate centers on two groups of
687 apparently contradictory observations: geometric and geomorphic evidence supporting recent
688 uplift, and extremely limited post-Cretaceous sedimentation and erosion arguing against a major
689 recent uplift event. Historically, most of the evidence for recent uplift was based on geomorphic
690 landforms that lacked quantitative dating (e.g., King, 1962 Partridge and Maud 1987), though
691 more recent work inverting river profile shapes also suggests recent uplift (Paul et al., 2014; G.
692 G. Roberts & White, 2010; Rudge et al., 2015). Terraces on the lower Orange River suggest 80-
693 100 m of post-Miocene incision, while upstream and the Vaal-Orange confluence they suggest
694 120-140 m of incision (M. C. J. de Wit, 1999). Shoreline geometries contained in offshore
695 stratigraphic architecture suggest continental uplift on the order of a few hundred meters at ~25
696 Ma on the east coast (Baby, Guillocheau, Boulogne, et al., 2018; Baby, Guillocheau, Morin, et
697 al., 2018), and Pliocene marine terraces have been uplifted to ~400 m above sea level near Port
698 Elizabeth (McMillan, 1990). In contrast, magnitudes of erosion since the Cretaceous are
699 negligible in some locations by the preservation of crater facies kimberlites (Scholtz, 1985;
700 Smith, 1986), and limited to less than 1-4 km by extensive low temperature thermochronology
701 (Brown et al., 2002, 2014; Flowers & Schoene, 2010; Gallagher & Brown, 1999a; Kounov et al.,
702 2009, 2013; Raab et al., 2005; Stanley et al., 2013, 2015; Stanley & Flowers, 2020; Tinker et al.,
703 2008b; Wildman et al., 2015, 2016, 2017). Quantitative evidence on erosion has shown that
704 erosion rates over the last ~2 Ma were slow based on cosmogenic nuclides (Bierman et al., 2014;

705 Chadwick et al., 2013; Decker et al., 2013; Dirks et al., 2016; Fleming et al., 1999; Kounov et
706 al., 2007). There is very limited offshore sedimentation in the Cenozoic, also suggesting low
707 erosion magnitudes on the continents (Baby et al., 2020; Baby, Guillocheau, Boulogne, et al.,
708 2018; Baby, Guillocheau, Morin, et al., 2018; Guillocheau et al., 2012; Rouby et al., 2009;
709 Tinker et al., 2008a), and near Cape Town, essentially no incision since the Miocene (D. L.
710 Roberts et al., 2013). Together this suggests either limited recent surface uplift or that almost no
711 erosion was caused by any recent uplift.

712 One way to reconcile these seemingly contrasting observations (geometric evidence for
713 recent uplift but very low erosion rates) is if surface uplift does not trigger a large erosional
714 response. The Hybrid Scenario model demonstrates that limited erosion in response to
715 substantial surface uplift is possible from a geomorphic standpoint. Normally, surface uplift is
716 thought to trigger an erosional response by steepening slopes and increasing stream power and
717 therefore erosion rates. In the case of the Hybrid Scenario, block uplift of an already low-relief
718 plateau only causes steepening in very focused locations in river channels. Therefore, even
719 though substantial topography is developed in the Cenozoic in the Hybrid Scenario, the erosional
720 response is subdued across most of the landscape, reconciling the low eroded volumes and
721 generally low erosion rates with geometric evidence for surface uplift.

722

723 5.3 Source-to-sink mass balance

724 The interest in topographic evolution, confined marine basins, and limited to absent
725 continental sediment storage in southern Africa make it an advantageous location to study source
726 to sink relationships. The extensive data coverage and the use of the landscape model to directly
727 calculate denudation magnitudes and thermochronology dates with an evolving crustal thermal
728 structure allows us to examine the source-to-sink mass balance more holistically than previously
729 possible. Past work compared estimated onshore denudation through time from AFT data to
730 marine sediment volumes on the west coast and the south coast with differing results. Rouby et
731 al. (2009) compared the marine sediment volumes from the west coast basins to AFT derived
732 denudation magnitudes for the western margin of southern Africa and Namibia (Gallagher and
733 Brown, 1999a, 1999b) and found a reasonably good match of the volumes through time with the
734 exception of the Cenozoic. On the southern margin, Tinker et al. (2008a, 2008b) compared the
735 AFT derived denudation and sediment volume in the Outeniqua Basin and found that the marine

736 sediment volumes were an order of magnitude less than onshore denudation volumes, though the
737 patterns timing of denudation and deposition match well (Tinker et al., 2008a). The marine
738 sediment volumes calculated by Tinker et al. (2008a) were based on only the shelf volumes, so
739 any material deposited in the deep sea was unaccounted for (Baby et al., 2020; Tinker et al.,
740 2008a). Richardson et al. (2017) estimated the eroded volume on the south coast using geometric
741 reconstruction of onshore sedimentary units and suggested that only one third to one half of the
742 eroded volume was contained in the Outeniqua Basin.

743 Our model provides a new way to examine this question by searching for erosion
744 histories that can match both the thermochronology data and the offshore sediment volumes.
745 There are several key parameters used to calculate thermochronology dates from erosion
746 histories, and by examining the ranges of these parameters that are able to satisfy both the
747 thermochronology and the sediment data we can gain insights into source to sink relationships.
748 Thermochronology is highly sensitive to the upper crustal thermal structure, and previous
749 thermochronology based denudation estimates (Gallagher & Brown, 1999a, 1999b; Tinker et al.,
750 2008b; Wildman et al., 2015, 2016) made some set of assumptions for this structure through
751 time, which could be a source of uncertainty when comparing onshore denudation and offshore
752 volumes. We calculate the thermal structure throughout the model run, and key parameters
753 controlling the structure are the temperature at the base of the model (T_{max}), the ratio between the
754 thermal diffusivity of the basement and the overlying Karoo sedimentary rocks (R_K). We vary
755 both T_{max} and R_K , as well as adding an additional non-thermal parameter which represents the
756 ratio of sediment volume lost between onshore erosion and offshore deposition (R_D). T_{max} can
757 range from 2400 to 5000°C (Table 2) which represents static geothermal gradients of 20-
758 42°C/km given the 120 km thick model, and R_K varies from 0.3 to 1 ranging from substantial
759 thermal blanketing by the Karoo sediments to no effect. Low misfit models converge with
760 thermal parameters suggesting higher static geothermal gradients (>34°C/km) and more extreme
761 thermal diffusivity ratios, where thermal diffusivity is 50% or less in the Karoo sediments as
762 compared with the basement (Fig. 4I, 4J). The combination of higher temperatures and the base
763 of the model and high thermal blanketing means that the low misfit models have higher
764 geothermal gradients in the upper crust, therefore requiring lower magnitudes of exhumation to
765 produce the observed thermochronology dates. Even with these values for the thermal

766 parameters, low misfit models converge on values of the deposition ration, R_D , where only $\frac{1}{2}$ to
767 $\frac{1}{4}$ of the eroded material is deposited in the basins (Fig 4K).

768 There are several caveats to this ratio, however. The first is that there are tradeoffs
769 between all of these parameters. More extreme geothermal gradients or thermal diffusivity ratios
770 (outside the range over which parameters were allowed to vary) would require less denudation to
771 satisfy the thermochronology data, yielding a lower mismatch between the predicted and
772 observed volumes. Additionally, while the predicted sediment volumes match the observed
773 sediment volumes well for certain times throughout the model run, particularly in the
774 Cretaceous, there are other times when the model predictions underestimate the volume of
775 sediment (Figure 7). Since at times the model underestimates the sediment volume, the ratio of
776 sediment loss implied by the parameter R_D in the low misfit models is likely an upper limit for
777 sediment loss. Also, in reality the ratio of sediment loss may have been variable through time
778 while R_D is fixed throughout a model run. Despite these caveats, the models suggest that more
779 material is eroded than deposited in the marine basins, perhaps greater than twice as much.

780 This, of course, begs the question of what happened to this “missing” sediment? We see
781 three possible explanations: 1) material was removed from the system via tectonic transport out
782 of the region, 2) material was removed from the system via oceanic transport out of the area, or
783 3) material was removed from the continent via chemical denudation and therefore not deposited
784 as a solid load in the basins. We favor this as evidence of substantial chemical denudation on the
785 continent, but we will examine the evidence for each of these mechanisms.

786 There is clear evidence that some material eroded off the southern coast during the early
787 portion of Gondwana breakup was deposited in the marine basins that are presently near the
788 Falkland Plateau, now situated in the SW Atlantic Ocean. In the Late Jurassic and Early
789 Cretaceous this basin was situated adjacent to the Outeniqua Basin (Baby, Guillocheau,
790 Boulogne, et al., 2018; R. V. Dingle & Scrutton, 1974; Macdonald et al., 2003; Martin et al.,
791 1982; Richardson et al., 2017; Williams, 2015). The North Falkland Basin contains continental
792 facies, likely derived from southern Africa (Baby, Guillocheau, Boulogne, et al., 2018;
793 Richardson et al., 2017; Williams, 2015). The main period of southern African deposition into
794 this basin was \sim 135-130 Ma, after which transform motion on the Agulhas-Falkland Fracture
795 Zone and eventual opening of the South Atlantic removed the North Falkland Basin from
796 proximity to southern Africa (Baby, Guillocheau, Boulogne, et al., 2018; R. V. Dingle &

797 Scrutton, 1974; Martin et al., 1982). Thus any sediment loss due to tectonic transport is limited to
798 the Early Cretaceous.

799 Several erosional features and contourites deposits present on all margins show that
800 sediments have been eroded and redistributed since the Lower Cretaceous by oceanic processes
801 (e.g., Baby, Guillocheau, Boulogne, et al., 2018; Hopkins, 2006; Thiéblemont et al., 2020;
802 Uenzelmann-Neben et al., 2007). Oceanic current structures have been characterized at various
803 depth since Aptian - Albian times (120-110 Ma) in Walvis and Zambezi Basins, but their role
804 became major during Early Miocene (23-16 Ma, Hopkins, 2006; Thiéblemont et al., 2020;
805 Uenzelmann-Neben et al., 2007). The ability of these oceanic currents to transport large volumes
806 of sediment (here during Neogene times) is difficult to quantify, even though it is of primary
807 importance in modeling source-to-sink systems. Concerning surficial currents, Orange River
808 sand is known to be transported up 1000+ km northward up the Namibian coast via littoral drift
809 (e.g., Garzanti et al., 2018) but the amount of sand transported is estimated at 1500-15000 km³
810 over the last 15 Myr (Garzanti et al., 2018) which only amounts to a small fraction of the west
811 coast sediment budget. In summary, the magnitude of sediment lost due to oceanic transport is
812 unknown. It may be significant, particularly in the Miocene, but sediment lost this way varies in
813 space and time.

814 Finally, chemical weathering on the continent could have been substantial. Basalts are
815 particularly susceptible to chemical weathering (e.g., Dessert et al., 2003; Dupré et al., 2003) and
816 much of the eroded material in the Cretaceous was Karoo flood basalts (e.g., Hanson et al., 2009;
817 Stanley et al., 2015; Tinker et al., 2008a). To add to that, Cretaceous erosion took place under
818 climatic conditions much warmer than today, which could have promoted chemical weathering
819 (e.g., Cohen et al., 2004; Jenkyns et al., 2004). A rough compilation of precipitation records
820 based on paleobotanical data suggests a sharp change around 85 Ma from semi-arid to very
821 humid conditions favoring intense silica weathering up to 40 Ma (Braun et al. 2014). Deep
822 weathering surfaces are found throughout southern Africa (e.g., Summerfield, 1983). North of
823 our study area, such weathering surfaces were dated in southern Congo (Katanga) based on
824 supergene manganese ore between to 77 Ma and 2 Ma with several peaks, demonstrating many
825 phases of weathering and surface formation since the Cretaceous (De Putter & Ruffet, 2020).
826 Within our study area there is evidence for the role of chemical weathering in the denudation
827 history in some locations (e.g., Chadwick et al., 2013; Margirier et al., 2019).

828 Overall, our model results suggest that a substantial volume of material eroded from the
829 continent was not accounted for in the sediment volumes presently in the marine basins. This
830 sediment loss was likely due to a combination of factors, and the most important process may
831 have varied through time. In the Early Cretaceous, sediment could have been deposited on the
832 Falkland Plateau (e.g., Baby, Guillocheau, Boulogne, et al., 2018; R. V. Dingle & Scrutton,
833 1974; Martin et al., 1982), while oceanic currents may have redistributed substantial volumes
834 especially in the Neogene (e.g., Thiéblemont et al., 2020; Uenzelmann-Neben et al., 2007) (e.g.,
835 Uenzelmann-Neben et al., 2017; Thiéblemont et al., 2020). Throughout the history, but
836 especially during the Late Cretaceous and Paleogene, substantial denudation may have occurred
837 via chemical processes resulting in less sediment deposited as a solid load in the basins. Our best
838 fitting models match the observed sediment volumes best in the Late Cretaceous (Fig 8) with
839 only $\sim 1/3$ of the eroded sediment being deposited in the basin. Climatic conditions were
840 favorable for chemical weathering at that time (e.g., Braun et al., 2014) and we take our results to
841 provide support for substantial continental chemical weathering in southern Africa, especially in
842 the Late Cretaceous and Paleogene.

843

844 5.4 Climate?

845 A weakness of our modelling approach is that we do not consider the role of climate or
846 precipitation changes through time. It is beyond the scope of this particular study to explore
847 those effects in full, but as a test to understand the magnitude of potential effects we ran an
848 additional inversion where we varied precipitation instead of uplift parameters. The goal of this
849 exercise was to test whether variations in precipitation alone could explain the observations. In
850 these models, initial topography was allowed to vary between 0 and 2000 m and then no other
851 uplift besides the isostatic response to erosion was imposed. This essentially is prescribing that
852 plateau uplift pre-dates the start of the model at 145 Ma. Precipitation rate was allowed to
853 increase by a factor of 0 to 100 for a period of 5 to 40 Myr in the Cretaceous, before returning to
854 the background rate, with an option of varying again by another factor from 0 to 100 in more
855 recent times (Table S3, Figure S1). This mirrors the structure of the uplift scenarios, but instead
856 varies precipitation rate (Figure 12, Table S3, Figure S1). In addition to precipitation rate, we
857 also allowed the erosional and thermal parameters varied in the uplift scenarios to vary.

858 This inversion converges on a parameter set that is able to reproduce the observations
859 with misfits <2 , a similar level to the two best-fitting scenarios for the uplift driven cases. Some
860 parameters are more tightly confined than others, but the lowest misfit models have ~ 1400 m of
861 initial topography, an increase in rainfall of >50 times the base rainfall starting at ~ 95 Ma and
862 lasting for 20 to 40 Myr before returning to the background value (Fig 12). This is followed by a
863 second uptick in precipitation by again >50 times background in the last 35 Myr. This suggests
864 that precipitation changes could potentially play an important role in the erosion history, but we
865 should first examine how realistic these results are.

866 Assuming a reference present-day rate of precipitation of 0.8 m/yr, an increase by a factor
867 of 50-100 would mean that the low misfit models require 40-80 m/yr of precipitation in the
868 Cretaceous. Maximum annual rainfall at present, globally, is on the order of 10 m/yr, so these
869 values seem unrealistically high, though the Cretaceous had a substantially different climate than
870 today. Global reconstructions suggest that climate in southern Africa was arid in the early to
871 mid-Cretaceous, moving toward humid starting at ~ 85 Ma to the end of the Cretaceous
872 (Chumakov et al., 1995; Hay & Floegel, 2012). Continental paleoprecipitation records derived
873 from southern Africa during the Cretaceous are unfortunately sparse, but fossil evidence from the
874 Atlantic coastal margin indicates progressive drying from ~ 130 to 90 Ma and a change from arid
875 or semi-arid conditions to humid at ~ 85 Ma (Bamford & Stevenson, 2002; Braun et al., 2014;
876 Sandersen, 2007). On the Indian coastal margin this transition began earlier, ~ 90 Ma (Ponte et
877 al., 2019). Limited evidence suggests humid conditions on the coastal plains until the beginning
878 of the present arid period, which began on the Atlantic margin ~ 15 Ma (Braun et al., 2014;
879 Pickford et al., 1999; Ponte et al., 2019; Senut et al., 2009). On the plateau surface fossil records
880 are limited to a kimberlite pipes which preserve crater lake sediments. These suggest different
881 conditions from the coastal plains with temperate to mildly humid conditions at ~ 95 -90 Ma
882 (Rayner et al., 1997) and dry temperate conditions at ~ 70 -65 Ma (Smith, 1986).

883 Evidence for wetting of the climate on the coastal plains in the mid-Cretaceous could be
884 consistent with the increase in precipitation rate required by the precipitation-driven models from
885 95-90 Ma. However, the observations suggest the climate transition on the Atlantic margin post-
886 dates the timing of increased rainfall in the model by 5-10 Myr, and it appears there were
887 different conditions on the plateau and the coastal plains. A 50x or more increase in rainfall
888 across the entire plateau is somewhat difficult to reconcile with the observations. There is also no

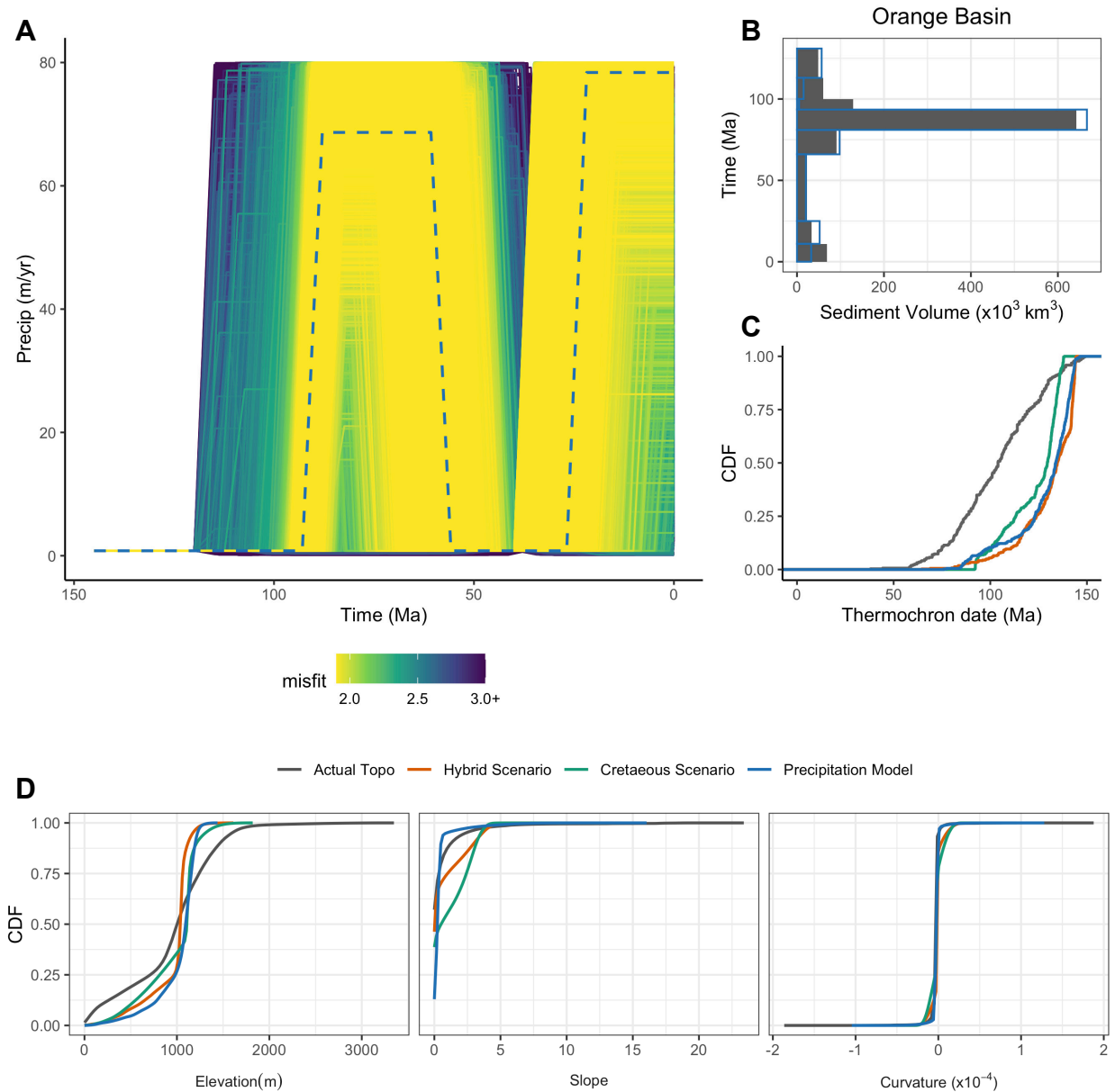


Figure 12. Results from precipitation variation inversion model. A) Paths showing precipitation magnitude over time for forward models, colored by misfit with yellow being good fits to the data. Blue dashed line shows best fit model. B) Comparison of the observed sedimentary flux in the Orange Basin (grey boxes) with predictions from the best fit precipitation-driven model (blue). C) Comparison of the CDFs for all published thermochronology dates (AFT and AHe, see Fig 2) with those predicted by all three best fit models - the Cretaceous Scenario (green), the Hybrid Scenario (red-orange), and the model driven only by precipitation (blue). D) Comparisons of the topographic metrics of the observed topography and all three best fit predictions.

890 obvious evidence for the marked decrease in rainfall in the models in the latest Cretaceous or
891 early Cenozoic, and the high rainfall amounts predicted by the model since the mid-Cenozoic are
892 also inconsistent with the dominantly semi-arid to arid conditions on most of the plateau today.

893 On the whole, while an extreme increase in rainfall can reproduce the observed
894 Cretaceous erosion pulse, it is not realistic as the sole driver for this erosion event. We interpret
895 these results to mean that while precipitation or climate changes likely played a role in southern
896 Africa's erosion and topographic history, they cannot realistically explain the magnitude of
897 erosion that is observed without any topographic uplift. This is in concert with geometric
898 evidence for continental uplift from marine archives that cannot be caused by changes in climate
899 alone (Baby et al., 2020; Baby, Guillocheau, Boulogne, et al., 2018). It is also worth noting that
900 changes in topographic conditions could cause changes in local climate and precipitation
901 conditions through orographic effects. For example, development of a plateau in the mid-
902 Cretaceous could induce a transition to wetter conditions on the coastal plateau margins and
903 maintain dryer conditions within the plateau interior, a scenario which is consistent with the
904 fossil record.

905

906 5.5 Distinguishing geodynamic mechanisms for plateau uplift

907 Both the Cretaceous Scenario and the Hybrid Scenario predict some topographic
908 development in the Cretaceous but the two scenarios differ in magnitude and the duration of
909 continental tilting during this uplift phase. We can compare the rates and magnitudes from our
910 models to those which might be expected from different geodynamic mechanisms for uplift.
911 Both models predict a total of ~1400 m of dynamic topography by the end of the model run. This
912 is within, but on the upper end, of the range of predicted magnitudes of present day dynamic
913 topography in southern Africa, though it should be noted that these predictions vary widely (e.g.,
914 Flament et al., 2013). However, the two scenarios differ in the timing and rate of topographic
915 development (Fig. 13). The Cretaceous Scenario has a much higher uplift magnitude during
916 dynamic tilting than the Hybrid scenarios (1414 m vs 482 m for their respective best fit models,
917 Fig. 13). We can also compare both vertical uplift rates and horizontal propagation rates. One of
918 the fixed parameters in all models is that the dynamic uplift occurs linearly over 5 Myr. The
919 Cretaceous Scenario then has a dynamic uplift rate of 0.28 mm/yr, while the Hybrid Scenario
920 uplifts at a rate of 0.1 mm/yr. To approximate the horizontal propagation rates for the uplift

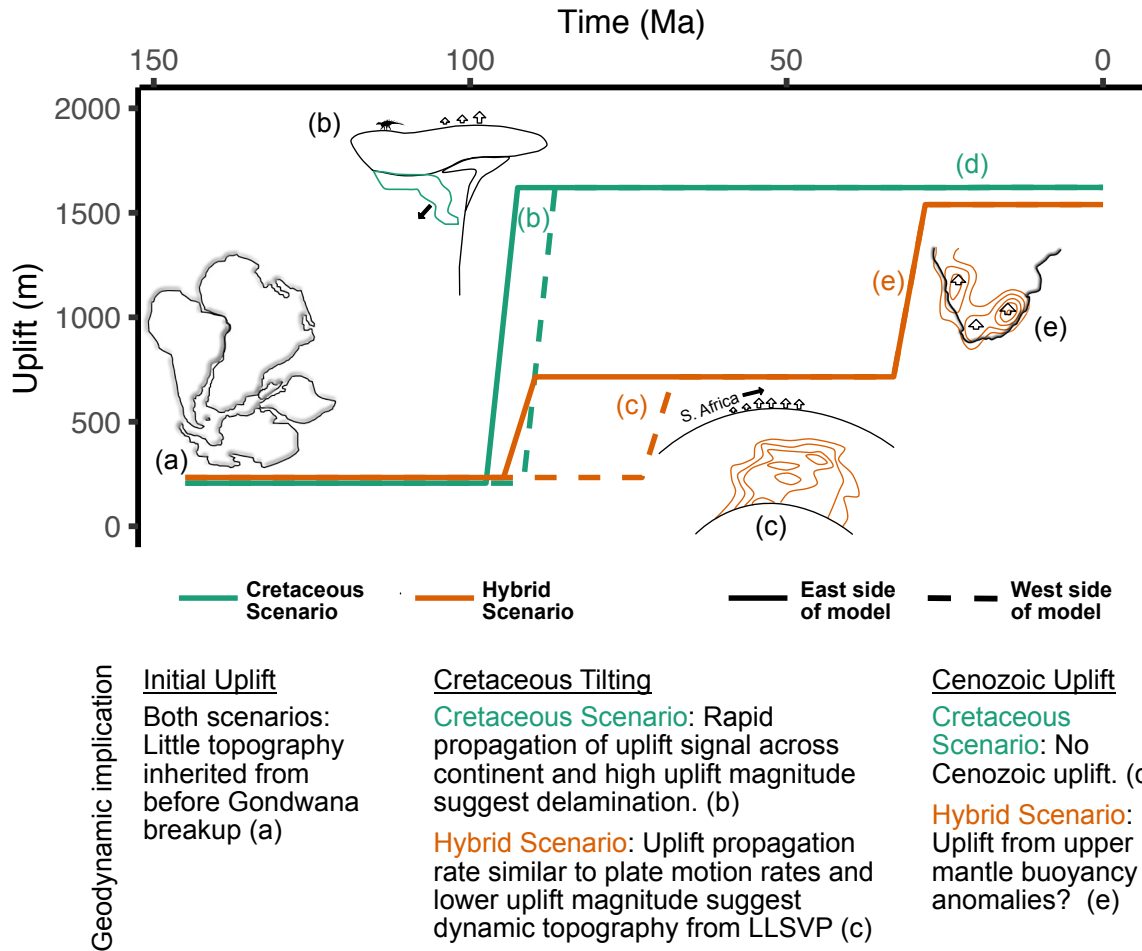


Figure 13. Geodynamic implications of the model results. Lines on graph show uplift over time for best fit models from the low misfit regions of model results. Cartoons show implied geodynamic mechanism for each uplift phase. See text for a more complete discussion and Table 1 for more on geodynamic hypotheses.

922 signal, we can use the tilt time parameter and the width of the model. The tilt time parameter is
923 the time delay between the east side of the model initiating uplift and the west side (Fig. 13). In
924 essence, it is the amount of time it takes the uplift to propagate across the model domain. A
925 rough estimate of the horizontal propagation rate that can be compared to plausible geodynamic
926 deformation rates is given by dividing the 2365 km wide model domain by the tilt time (5.9 Myr
927 for the best fit Cretaceous Scenario and 21.7 Myr for the best fit Hybrid Scenario). The
928 propagation rate of the uplift is then 40 cm/yr for the Cretaceous Scenario and 11 cm/yr in the
929 Hybrid Scenario.

930 Braun et al. (2014) proposed that tilting and dynamic uplift of the plateau was caused by
931 movement of the African plate over the LLSVP in the deep mantle. In this conceptual model,
932 rates of horizontal propagation should be set by plate motion rates. Both the Cretaceous and
933 Cenozoic propagation rates are fast for plate motion rates, but the Cretaceous Scenario especially
934 so. Plate motion rates reconstructed for Africa in the mid-Cretaceous vary. Colli et al. (2014)
935 reconstructed absolute plate speeds for a point in the northwest quadrant of our model (27°S,
936 15°E) using the Müller et al. (1993) fixed hotspot reference frame and a combination of the
937 O'Neill et al. (2005) and Steinberger and Torsvik (2008) moving hotspot and true polar wander
938 models. The fixed hotspot frame gave velocities increasing from <1 to ~3 cm/yr from 110 to 90
939 Ma (Colli et al., 2014; Müller et al., 1993), while the moving hotspot and true polar wander
940 models gave velocities ranging from ~2 to 4 cm/yr between 110 and 90 Ma with a major spike to
941 >10 cm/yr between 105 and 100 Ma (Colli et al., 2014; O'Neill et al., 2005; Steinberger &
942 Torsvik, 2008). These rates are all substantially below the 40 cm/yr predicted by the Cretaceous
943 Scenario but begin to approach those of the 11 cm/yr predicted by the Hybrid Scenario at times.

944 In addition to propagation rates that are too fast to be dictated by plate motion of southern
945 Africa riding over the LLSVP, the Cretaceous Scenario requires a high magnitude of Cretaceous
946 topography, ~1400 m. While initial work suggested that this magnitude of dynamic topography
947 could be attributed to the LLSVP (e.g., Lithgow-Bertelloni & Silver, 1998), more recent studies
948 suggest that the large degree-two lower mantle structures have a more limited influence on
949 dynamic topography at the surface (Hoggard et al., 2016; Osei Tutu et al., 2018; Steinberger,
950 2016; Steinberger et al., 2019; Watkins & Conrad, 2018). Together, this implies that if the
951 Cretaceous Scenario is the correct model, some other mechanism beyond dynamic topography
952 over the LLSVP needs to be invoked to explain the rapidity and magnitude of elevation gain.

953 Removal of mantle lithosphere either through delamination or dripping of convective instabilities
954 could potentially generate these magnitudes and rates. Hu et al. (2018) proposed a delamination-
955 style peeling back of the lowermost lithosphere triggered by motion over hotspots, also implying
956 that rates would dominantly be controlled by plate motion rates. However, at least for
957 lithospheric drips, dynamic models show that once instabilities form, they can grow
958 exponentially or even super exponentially depending on the wavelength of the perturbation and
959 the viscosity structure (e.g., Conrad & Molnar, 1997; Molnar et al., 1998). So perhaps once
960 destabilized the dense lower lithosphere could have been removed fairly rapidly. Dripping or
961 delamination can also produce surface uplift on the order of 1-2 km (e.g., Göğüş & Pysklywec,
962 2008a, 2008b) in line with the uplift required by our Cretaceous Scenario. There is also evidence
963 for Cretaceous lithospheric perturbation in southern Africa from elevated geothermal gradients
964 recorded by mantle and lower crustal xenoliths (Bell et al., 2003; Schmitz & Bowring, 2003) and
965 the coincidence of a major erosion phase with this warming geotherm (Stanley et al., 2013). If
966 the Cretaceous Scenario is correct, we suggest much of the uplift of southern Africa was driven
967 by lithospheric foundering rather than solely sublithospheric dynamic topography (Fig. 13).

968 The Hybrid Scenario has smaller magnitudes (400-500 m) of dynamic topography in the
969 Cretaceous and propagation rates that are more consistent with plate motion reconstructions,
970 followed by ~800 m of uplift in the Cenozoic. Retrodictions of dynamic topography back
971 through the Cretaceous are somewhat limited, but several predict the development of 200-500 m
972 of dynamic topography during the early Late Cretaceous, due to motion over the LLSVP and/or
973 motion away from the South American subduction zone (Flament et al., 2014; Rubey et al.,
974 2017; Zhang et al., 2012). Motion of southern Africa over the LLSVP and deep-mantle derived
975 dynamic topography seems to provide a suitable explanation for the magnitudes and rates of
976 Cretaceous topographic development in the Hybrid Scenario (Fig. 13). Interestingly, the peak in
977 southern African plate motion rate in the moving hotspot/true polar wander reference frame
978 (Colli et al., 2014; O'Neill et al., 2005; Steinberger & Torsvik, 2008) most closely corresponds
979 with the rates in the Hybrid Scenario and also coincides with the initiation of Cretaceous uplift.
980 Colli et al. (2014) argued that changes in South Atlantic spreading velocities are related to
981 topographic changes on the continents through pressure driven flow in the asthenosphere.
982 Together this highlights the potential links between the deep earth, plate motions, and continental
983 erosion. An additional ~800 m of Cenozoic dynamic topography in the Hybrid Scenario onsets at

984 30-35 Ma. This also coincides with a rapid phase of south Atlantic spreading (Colli et al., 2014),
985 as well as the proposed timing for development of small-scale convection beneath Africa (Burke,
986 1996), and overlaps with development of the East Africa Rift system (e.g., Ebinger & Sleep,
987 1998; E. M. Roberts et al., 2012). Development of this Cenozoic topography seems more likely
988 to be derived from upper mantle density anomalies than the LLSVP, though both could
989 contribute (Hoggard et al., 2016; Winterbourne et al., 2009).

990 The Hybrid and Cretaceous Scenarios have different magnitudes and rates of uplift,
991 implying different driving mechanisms for uplift (Fig. 13). We do not strongly favor one over the
992 other but note that an area for future work could be to compare our low misfit models directly
993 with geodynamic models, particularly since the driver for dynamic topography in the landscape
994 model is a basal stress.

995

996 **6. Conclusions**

997 We used inversion methods to compare landscape models varying a range of uplift,
998 erosion, and thermal parameters with observed offshore sediment volumes, thermochronology
999 data, and topography from Southern Africa. We explored three proposed hypotheses for when
1000 the plateau was elevated and found good matches to two possible uplift histories (Fig. 3). One
1001 suitable model has plateau development entirely in the Cretaceous, with ~1400 m of dynamic
1002 uplift and continental tilting over ~6 Ma between 100 and 90 Ma. The other suitable model has
1003 two phase plateau development with ~500 m of dynamic uplift and continental tilting from ~100-
1004 75 Ma followed by ~800 m of dynamic block uplift at ~30 Ma (Fig. 5). The data that we used
1005 cannot distinguish between these two uplift histories, though stratigraphic architecture at the
1006 margins suggests two phases of uplift (Baby et al., 2020; Baby, Guillocheau, Boulogne, et al.,
1007 2018; Baby, Guillocheau, Morin, et al., 2018). However, model predictions can be used to
1008 identify data that could be used to differentiate between these model predictions. For example,
1009 the best fit models for each uplift history differ markedly in both the rates and patterns predicted
1010 for erosion rates over the last 1 Myr, and studies could be designed to target areas of expected
1011 differences using cosmogenic radionuclides (Fig. 10).

1012 Results from these models give some insight into the link between erosion rate, uplift,
1013 and topography in southern Africa. Good fitting models show an important relationship between
1014 the magnitudes of the erosivity constant, K_f , and our parameterization of an erosion threshold, ε_c

1015 (Fig. 6). This suggests that a fairly high threshold is important for maintaining uplifted
1016 topography over long periods of geologic time with low erosion and sedimentation rates. In
1017 addition to the erosive parameters, the erosional response to uplift is highly sensitive to the shape
1018 of the uplift. Our models show that continental scale tilting can cause a high magnitude erosional
1019 response for a range of uplift amounts due to steepening of the entire drainage network and
1020 stability or enhancement of large drainages. This is in line with previous work (Braun et al.,
1021 2013, 2014) and is important for reproducing the pulsed nature of Cretaceous erosion and
1022 sedimentation in southern Africa. In contrast, the block uplift shape produces a relatively small
1023 erosional response for significant magnitudes of uplift because much of the plateau interior does
1024 not steepen (Fig. 11). These conditions are able to reconcile geometric evidence for Cenozoic
1025 uplift with the observed low magnitudes of erosion.

1026 Source to sink mass balance between the amount of material eroded implied by the
1027 thermochronology data and the amount deposited in the offshore basins suggests a substantial
1028 amount of mass loss. Best-fit models suggest about 3 times as much material was eroded as
1029 deposited. While some material could have been transported away by ocean currents or tectonics
1030 (Garzanti et al., 2018; Richardson et al., 2017), we argue that this is evidence for substantial
1031 chemical denudation, where a large portion of the material removed from the continent was
1032 transported in solution to the ocean and therefore not directly deposited in marine basins. This
1033 has potential implications for climate and the nature of cratonic erosion that could be explored
1034 further with future work.

1035 We did not vary climate or precipitation in our models, but to test the extent to which this
1036 could affect the results we ran one additional inversion where no uplift was imposed on the
1037 model, but precipitation magnitude was allowed to vary through time. We found some
1038 precipitation-only models were able to match the observed data as well as the uplift driven
1039 models, but only if average precipitation ranged over two orders of magnitude up to
1040 unrealistically high amounts (Fig. 12). Precipitation variability could have played an important
1041 role in southern Africa's erosion history, but it cannot realistically explain the observations
1042 without topographic uplift. The relative roles of these processes in southern Africa merits more
1043 exploration in the future.

1044 Finally, while the data cannot distinguish between the Cretaceous and Cenozoic best fit
1045 models at the present, the relative rates of deformation and magnitudes of surface change might

1046 help discriminate between the geodynamic mechanisms which could be driving them (Fig. 13).
1047 For the Cretaceous Scenario, the propagation of the uplift signal during continental tilting is
1048 likely too rapid to be only related to plate tectonic motion, and uplift magnitudes are higher than
1049 expected for dynamic uplift due to the LLSVP. Uplift in this case may be more likely to be
1050 driven by processes that can act faster and cause more surface change like delamination (e.g.,
1051 Göğüş & Pysklywec, 2008b; Hu et al., 2018) than by the African Plate moving over the LLSVP
1052 (Braun et al., 2014). However, in the Hybrid Scenario uplift propagates across the continent at a
1053 rate more in line with plate motions, and uplift magnitudes are lower. Thus, tilting as the African
1054 Plate rides over the LLSVP is a highly plausible uplift mechanism. Geodynamic models could be
1055 directly compared to, or even constrained by the results presented here.

1056 **Acknowledgments, Samples, and Data**

1057 Support for this project was provided by the Alexander von Humboldt Foundation. We thank
1058 Lukas Becker for reading an early version of the manuscript and members of the Earth Surface
1059 Processes Modelling group at the GFZ for helpful feedback and discussions. Many figures were
1060 made using the R packages ggplot2 (Wickham, 2016), tmap (Tennekes, 2018), and rayshader
1061 (Morgan-Wall, 2020). All data included in the modelling has been previously published and is
1062 available in Amante & Eakins (2009), Baby et al. (2020), Belton & Raab (2010), Brown et al
1063 (1990 2002, 2014), Flowers & Schoene (2010), Green et al. (2017), Kounov et al. (2009, 2013),
1064 Raab et al. (2002), Stanley et al. (2013, 2015), Stanley & Flowers (2020) Tinker et al. (2008b),
1065 and Wildman et al. (2015, 2016, 2016). Data is summarized with publication information
1066 specified for individual data points in the supplemental materials. Code used to generate all
1067 model results is archived with Zenodo (Braun & Stanley, 2020) as is all of the input data,
1068 configuration, and results (Stanley, 2020).

1069

1070 **References**

- 1071 Al-Hajri, Y., White, N., & Fishwick, S. (2009). Scales of transient convective support beneath
1072 Africa. *Geology*, 37(10), 883–886. <https://doi.org/10/fst5pn>
- 1073 Amante, C., & Eakins, B. W. (2009). ETOPO1 arc-minute global relief model: procedures, data
1074 sources and analysis.

- 1075 Baby, G. (2017). Mouvements verticaux des marges passives d’Afrique australe depuis 130 Ma,
 1076 étude couplée: stratigraphie de bassin: analyse des formes du relief.
- 1077 Baby, G., Guillocheau, F., Morin, J., Ressouche, J., Robin, C., Broucke, O., & Dall’Asta, M.
 1078 (2018). Post-rift stratigraphic evolution of the Atlantic margin of Namibia and South
 1079 Africa: Implications for the vertical movements of the margin and the uplift history of the
 1080 South African Plateau. *Marine and Petroleum Geology*, *97*, 169–191.
 1081 <https://doi.org/10/gfnc2j>
- 1082 Baby, G., Guillocheau, F., Boulogne, C., Robin, C., & Dall’Asta, M. (2018). Uplift history of a
 1083 transform continental margin revealed by the stratigraphic record: The case of the
 1084 Agulhas transform margin along the Southern African Plateau. *Tectonophysics*, *731–732*,
 1085 104–130. <https://doi.org/10/gg6wn2>
- 1086 Baby, G., Guillocheau, F., Braun, J., Robin, C., & Dall’Asta, M. (2020). Solid sedimentation
 1087 rates history of the Southern African continental margins: Implications for the uplift
 1088 history of the South African Plateau. *Terra Nova*, *32*(1), 53–65.
 1089 <https://doi.org/10/ggw55p>
- 1090 Bamford, M. K., & Stevenson, I. R. (2002). A submerged Late Cretaceous podocarpaceous
 1091 forest, west coast, South Africa : research letter. *South African Journal of Science*, *98*(3–
 1092 4), 181–185.
- 1093 Barnhart, K. R., Tucker, G. E., Doty, S., Shobe, C. M., Glade, R. C., Rossi, M. W., & Hill, M. C.
 1094 (2020). Inverting topography for landscape evolution model process representation: Part
 1095 2, calibration and validation. *Journal of Geophysical Research: Earth Surface*, *n/a*(*n/a*),
 1096 e2018JF004963. <https://doi.org/10/ggnf59>
- 1097 Bell, D. R., Schmitz, M. D., & Janney, P. E. (2003). Mesozoic thermal evolution of the southern
 1098 African mantle lithosphere. *Lithos*, *71*(2–4), 273–287. <https://doi.org/10/chzs66>
- 1099 Belton, D. X., & Raab, M. J. (2010). Cretaceous reactivation and intensified erosion in the
 1100 Archean–Proterozoic Limpopo Belt, demonstrated by apatite fission track
 1101 thermochronology. *Tectonophysics*, *480*(1–4), 99–108. <https://doi.org/10/fwqqqs>
- 1102 Bierman, P. R., Coppersmith, R., Hanson, K., Neveling, J., Portenga, E. W., & Rood, D. H.
 1103 (2014). A cosmogenic view of erosion, relief generation, and the age of faulting in
 1104 southern Africa. *GSA Today*, *24*(9), 4–11. <https://doi.org/10/gg6w2n>

- 1105 Bluck, B. J., Ward, J. D., & De Wit, M. C. J. (2005). Diamond mega-placers: southern Africa
 1106 and the Kaapvaal craton in a global context. *Geological Society, London, Special*
 1107 *Publications*, 248(1), 213–245. <https://doi.org/10/bbmgfj>
- 1108 Braun, J. (2002). Quantifying the effect of recent relief changes on age–elevation relationships.
 1109 *Earth and Planetary Science Letters*, 200(3), 331–343. <https://doi.org/10/fkcnn8>
- 1110 Braun, J. (2018). A review of numerical modeling studies of passive margin escarpments leading
 1111 to a new analytical expression for the rate of escarpment migration velocity. *Gondwana*
 1112 *Research*, 53, 209–224. <https://doi.org/10/gdb743>
- 1113 Braun, J., & Stanley, J. R. (2020). FastScape landscape evolution model, fortran version utilized
 1114 for southern African model inversions. Zenodo. <http://doi.org/10.5281/zenodo.4150333>
- 1115 Braun, J., & Willett, S. D. (2013). A very efficient O (n), implicit and parallel method to solve
 1116 the stream power equation governing fluvial incision and landscape evolution.
 1117 *Geomorphology*, 180, 170–179. <https://doi.org/10/gbcbc9>
- 1118 Braun, J., Van Der Beek, P., & Batt, G. (2006). *Quantitative thermochronology: numerical*
 1119 *methods for the interpretation of thermochronological data*. Cambridge University Press.
- 1120 Braun, J., Robert, X., & Simon-Labric, T. (2013). Eroding dynamic topography. *Geophysical*
 1121 *Research Letters*, 40(8), 1494–1499. <https://doi.org/10/gcpz7w>
- 1122 Braun, J., Guillocheau, F., Robin, C., Baby, G., & Jelsma, H. (2014). Rapid erosion of the
 1123 Southern African Plateau as it climbs over a mantle superswell. *Journal of Geophysical*
 1124 *Research: Solid Earth*, 119(7), 6093–6112. <https://doi.org/10/ggfrck>
- 1125 ten Brink, U., & Stern, T. (1992). Rift flank uplifts and Hinterland Basins: Comparison of the
 1126 Transantarctic Mountains with the Great Escarpment of southern Africa. *Journal of*
 1127 *Geophysical Research: Solid Earth*, 97(B1), 569–585. <https://doi.org/10/ckspp3>
- 1128 Brown, R. W., Rust, D. J., Summerfield, M. A., Gleadow, A. J., & De Wit, M. C. (1990). An
 1129 Early Cretaceous phase of accelerated erosion on the south-western margin of Africa:
 1130 Evidence from apatite fission track analysis and the offshore sedimentary record.
 1131 *International Journal of Radiation Applications and Instrumentation. Part D. Nuclear*
 1132 *Tracks and Radiation Measurements*, 17(3), 339–350. <https://doi.org/10/b7sq7r>
- 1133 Brown, R. W., Summerfield, M. A., & Gleadow, A. J. W. (2002). Denudational history along a
 1134 transect across the Drakensberg Escarpment of southern Africa derived from apatite
 1135 fission track thermochronology: DENUDATIONAL HISTORY OF THE

- 1136 DRAKENSBERG ESCARPMENT. *Journal of Geophysical Research: Solid Earth*,
 1137 107(B12), ETG 10-1-ETG 10-18. <https://doi.org/10/dd579x>
- 1138 Brown, R. W., Summerfield, M., Gleadow, A., Gallagher, K., Carter, A., Beucher, R., &
 1139 Wildman, M. (2014). Intracontinental deformation in southern Africa during the Late
 1140 Cretaceous. *Journal of African Earth Sciences*, 100, 20–41. <https://doi.org/10/f6rd48>
- 1141 Burke, K. (1996). The african plate. *South African Journal of Geology*, 99(4), 341–409.
- 1142 Burke, K., & Gunnell, Y. (2008). *The African erosion surface: a continental-scale synthesis of*
 1143 *geomorphology, tectonics, and environmental change over the past 180 million years*
 1144 (Vol. 201). Geological Society of America.
- 1145 Burke, K., & Wilson, J. T. (1972). Is the African Plate Stationary? *Nature*, 239(5372), 387–389.
 1146 <https://doi.org/10/frb9xw>
- 1147 Catuneanu, O., Wopfner, H., Eriksson, P. G., Cairncross, B., Rubidge, B. S., Smith, R. M. H., &
 1148 Hancox, P. J. (2005). The Karoo basins of south-central Africa. *Journal of African Earth*
 1149 *Sciences*, 43(1–3), 211–253. <https://doi.org/10/br73kj>
- 1150 Chadwick, O. A., Roering, J. J., Heimsath, A. M., Levick, S. R., Asner, G. P., & Khomo, L.
 1151 (2013). Shaping post-orogenic landscapes by climate and chemical weathering. *Geology*,
 1152 41(11), 1171–1174. <https://doi.org/10/gg6p2q>
- 1153 Chumakov, N. M., Zharkov, M. A., Herman, A. B., Doludenko, M. P., Kalandadze, N. N.,
 1154 Lebedev, E. L., et al. (1995). Climatic Belts of the Mid-Cretaceous Time. *Stratigraphy*
 1155 *and Geological Correlation*, 3(3), 42–63.
- 1156 Cockburn, H. A. P., Seidl, M. A., & Summerfield, M. A. (1999). Quantifying denudation rates
 1157 on inselbergs in the central Namib Desert using in situ–produced cosmogenic ¹⁰Be and
 1158 ²⁶Al. *Geology*, 27(5), 399–402. <https://doi.org/10/c9nmqx>
- 1159 Cockburn, H. A. P., Brown, R. W., Summerfield, M. A., & Seidl, M. A. (2000). Quantifying
 1160 passive margin denudation and landscape development using a combined fission-track
 1161 thermochronology and cosmogenic isotope analysis approach. *Earth and Planetary*
 1162 *Science Letters*, 179(3), 429–435. <https://doi.org/10/dmssc4>
- 1163 Cohen, A. S., Coe, A. L., Harding, S. M., & Schwark, L. (2004). Osmium isotope evidence for
 1164 the regulation of atmospheric CO₂ by continental weathering. *Geology*, 32(2), 157–160.
 1165 <https://doi.org/10/bcs23h>

- 1166 Colli, L., Stotz, I., Bunge, H.-P., Smethurst, M., Clark, S., Iaffaldano, G., et al. (2014). Rapid
1167 South Atlantic spreading changes and coeval vertical motion in surrounding continents:
1168 Evidence for temporal changes of pressure-driven upper mantle flow. *Tectonics*, 33(7),
1169 1304–1321. <https://doi.org/10/ggtgh5>
- 1170 Conrad, C. P., & Molnar, P. (1997). The growth of Rayleigh—Taylor-type instabilities in the
1171 lithosphere for various rheological and density structures. *Geophysical Journal
1172 International*, 129(1), 95–112. <https://doi.org/10/cqzqbw>
- 1173 Cordonnier, G., Bovy, B., & Braun, J. (2019). A versatile, linear complexity algorithm for flow
1174 routing in topographies with depressions. *Earth Surface Dynamics*, 7(2), 549–562.
1175 <https://doi.org/10/ggk9xb>
- 1176 Cox, K. G. (1989). The role of mantle plumes in the development of continental drainage
1177 patterns. *Nature*, 342(6252), 873–877. <https://doi.org/10/fd34f6>
- 1178 Croissant, T., & Braun, J. (2014). Constraining the stream power law: a novel approach
1179 combining a landscape evolution model and an inversion method. *Earth Surface
1180 Dynamics*, 2(1), 155–166. <https://doi.org/10/gb9b78>
- 1181 Crowley, K. d, Cameron, M., & Schaefer, R. l. (1991). Experimental studies of annealing of
1182 etched fission tracks in fluorapatite. *Geochimica et Cosmochimica Acta*, 55(5), 1449–
1183 1465. <https://doi.org/10/ckh6js>
- 1184 Dauteuil, O., Bessin, P., & Guillocheau, F. (2015). Topographic growth around the Orange River
1185 valley, southern Africa: A Cenozoic record of crustal deformation and climatic change.
1186 *Geomorphology*, 233, 5–19. <https://doi.org/10/gg6w26>
- 1187 De Putter, T., & Ruffet, G. (2020). Supergene manganese ore records 75 Myr-long Campanian to
1188 Pleistocene geodynamic evolution and weathering history of the Central African Great
1189 Lakes Region—Tectonics drives, climate assists. *Gondwana Research*.
1190 <https://doi.org/10/ghdn68>
- 1191 De Wit, M. C. J. (1988). Aspects of the geomorphology of the north-western Cape, South Africa.
1192 In *Geomorphological Studies in Southern Africa* (pp. 57–69). Rotterdam, Netherlands:
1193 CRC Press.
- 1194 Decker, J. E., Niedermann, S., & de Wit, M. J. (2013). Climatically influenced denudation rates
1195 of the southern African plateau: Clues to solving a geomorphic paradox. *Geomorphology*,
1196 190, 48–60. <https://doi.org/10/f4wwbs>

- 1197 Dessert, C., Dupré, B., Gaillardet, J., François, L. M., & Allègre, C. J. (2003). Basalt weathering
 1198 laws and the impact of basalt weathering on the global carbon cycle. *Chemical Geology*,
 1199 202(3–4), 257–273. <https://doi.org/10/crx35j>
- 1200 Dietrich, P., & Hofmann, A. (2019). Ice-margin fluctuation sequences and grounding zone
 1201 wedges: The record of the Late Palaeozoic Ice Age in the eastern Karoo Basin (Dwyka
 1202 Group, South Africa). *The Depositional Record*, 5(2), 247–271. <https://doi.org/10/ghdn6x>
- 1203 Ding, X., Salles, T., Flament, N., Mallard, C., & Rey, P. F. (2019). Drainage and Sedimentary
 1204 Responses to Dynamic Topography. *Geophysical Research Letters*, 46(24), 14385–
 1205 14394. <https://doi.org/10/ggj9vp>
- 1206 Dingle, R., & Hendry, Q. (1984). Late Mesozoic and Tertiary sediment supply to the eastern
 1207 Cape Basin (SE Atlantic) and palaeo-drainage systems in southwestern Africa. *Marine
 1208 Geology*, 56(1–4), 13–26. <https://doi.org/10/c86r5c>
- 1209 Dingle, R. V., & Scrutton, R. A. (1974). Continental Breakup and the Development of Post-
 1210 Paleozoic Sedimentary Basins around Southern Africa. *GSA Bulletin*, 85(9), 1467–1474.
 1211 <https://doi.org/10/dw2dq8>
- 1212 Dirks, P. H. G. M., Placzek, C. J., Fink, D., Dosseto, A., & Roberts, E. (2016). Using ¹⁰Be
 1213 cosmogenic isotopes to estimate erosion rates and landscape changes during the Plio-
 1214 Pleistocene in the Cradle of Humankind, South Africa. *Journal of Human Evolution*, 96,
 1215 19–34. <https://doi.org/10/f8trm3>
- 1216 Dixey, F. (1955). Some aspects of the geomorphology of central and southern Africa. Geological
 1217 Society of South Africa.
- 1218 Doucouré, C. M., & de Wit, M. J. (2003). Old inherited origin for the present near-bimodal
 1219 topography of Africa. *Journal of African Earth Sciences*, 36(4), 371–388.
 1220 <https://doi.org/10/bxn5zr>
- 1221 Doucouré, C. M., Wit, M. J. de, & Mushayandebvu, M. F. (1996). Effective elastic thickness of
 1222 the continental lithosphere in South Africa. *Journal of Geophysical Research: Solid
 1223 Earth*, 101(B5), 11291–11303. <https://doi.org/10/d7t9q8>
- 1224 Duncan, R. A., Hooper, P. R., Rehacek, J., Marsh, J. S., & Duncan, A. R. (1997). The timing and
 1225 duration of the Karoo igneous event, southern Gondwana. *Journal of Geophysical
 1226 Research: Solid Earth*, 102(B8), 18127–18138. <https://doi.org/10/fgs8g6>

- 1227 Dupré, B., Dessert, C., Oliva, P., Goddéri, Y., Viers, J., François, L., et al. (2003). Rivers,
1228 chemical weathering and Earth's climate. *Comptes Rendus Geoscience*, 335(16), 1141–
1229 1160. <https://doi.org/10/c9sz48>
- 1230 Ebinger, C. J., & Sleep, N. H. (1998). Cenozoic magmatism throughout east Africa resulting
1231 from impact of a single plume. *Nature*, 395(6704), 788–791. <https://doi.org/10/cjqczh>
- 1232 Erlanger, E. D., Granger, D. E., & Gibbon, R. J. (2012). Rock uplift rates in South Africa from
1233 isochron burial dating of fluvial and marine terraces. *Geology*, 40(11), 1019–1022.
1234 <https://doi.org/10/gg6w2v>
- 1235 Farley, K. (2000). Helium diffusion from apatite: General behavior as illustrated by Durango
1236 fluorapatite. *Journal of Geophysical Research: Solid Earth*, 105(B2), 2903–2914.
1237 <https://doi.org/10/cgf34w>
- 1238 Flament, N., Gurnis, M., & Müller, R. D. (2013). A review of observations and models of
1239 dynamic topography. *Lithosphere*, 5(2), 189–210. <https://doi.org/10/f46573>
- 1240 Flament, N., Gurnis, M., Williams, S., Seton, M., Skogseid, J., Heine, C., & Dietmar Müller, R.
1241 (2014). Topographic asymmetry of the South Atlantic from global models of mantle flow
1242 and lithospheric stretching. *Earth and Planetary Science Letters*, 387, 107–119.
1243 <https://doi.org/10/gg3hzz>
- 1244 Fleming, A., Summerfield, M. A., Stone, J. O., Fifield, L. K., & Cresswell, R. G. (1999).
1245 Denudation rates for the southern Drakensberg escarpment, SE Africa, derived from in-
1246 situ-produced cosmogenic ³⁶C1: initial results. *Journal of the Geological Society*,
1247 156(2), 209–212. <https://doi.org/10/cmdjtb>
- 1248 Flowers, R. M., & Schoene, B. (2010). (U-Th)/He thermochronometry constraints on unroofing
1249 of the eastern Kaapvaal craton and significance for uplift of the southern African Plateau.
1250 *Geology*, 38(9), 827–830. <https://doi.org/10/bptpcp>
- 1251 Flowers, R. M., Ketcham, R. A., Shuster, D. L., & Farley, K. A. (2009). Apatite (U–Th)/He
1252 thermochronometry using a radiation damage accumulation and annealing model.
1253 *Geochimica et Cosmochimica Acta*, 73(8), 2347–2365. <https://doi.org/10/ffkmvz>
- 1254 Gallagher, K., & Brown, R. W. (1999a). Denudation and uplift at passive margins: the record on
1255 the Atlantic Margin of southern Africa. *Philosophical Transactions of the Royal Society
1256 of London. Series A: Mathematical, Physical and Engineering Sciences*, 357(1753), 835–
1257 859. <https://doi.org/10/ckc9sq>

- 1258 Gallagher, K., & Brown, R. W. (1999b). The Mesozoic denudation history of the Atlantic
 1259 margins of southern Africa and southeast Brazil and the relationship to offshore
 1260 sedimentation. *Geological Society, London, Special Publications*, 153(1), 41–53.
 1261 <https://doi.org/10.1144/GSL.SP.1999.153.01.03>
- 1262 Garzanti, E., Dinis, P., Vermeesch, P., Andò, S., Hahn, A., Huvi, J., et al. (2018). Sedimentary
 1263 processes controlling ultralong cells of littoral transport: Placer formation and termination
 1264 of the Orange sand highway in southern Angola. *Sedimentology*, 65(2), 431–460.
 1265 <https://doi.org/10/gcvdp9>
- 1266 Gilchrist, A. R., & Summerfield, M. A. (1990). Differential denudation and flexural isostasy in
 1267 formation of rifted-margin upwarps. *Nature*, 346(6286), 739–742.
 1268 <https://doi.org/10/bc9dsp>
- 1269 Gilchrist, A. R., Kooi, H., & Beaumont, C. (1994). Post-Gondwana geomorphic evolution of
 1270 southwestern Africa: Implications for the controls on landscape development from
 1271 observations and numerical experiments. *Journal of Geophysical Research: Solid Earth*,
 1272 99(B6), 12211–12228. <https://doi.org/10/cknczm>
- 1273 Glotzbach, C., Paape, A., Baade, J., Reinwarth, B., Rowntree, K., & Miller, J. (2016). Cenozoic
 1274 landscape evolution of the Kruger National Park as derived from cosmogenic nuclide
 1275 analyses. *Terra Nova*, 28(5), 316–322. <https://doi.org/10/f858tb>
- 1276 Göğüş, O. H., & Pysklywec, R. N. (2008a). Mantle lithosphere delamination driving plateau
 1277 uplift and synconvergent extension in eastern Anatolia. *Geology*, 36(9), 723–726.
 1278 <https://doi.org/10/c7pnrr>
- 1279 Göğüş, O. H., & Pysklywec, R. N. (2008b). Near-surface diagnostics of dripping or delaminating
 1280 lithosphere. *Journal of Geophysical Research: Solid Earth*, 113(B11).
 1281 <https://doi.org/10/bndzss>
- 1282 Green, P. F., Duddy, I., Gleadow, A., Tingate, P., & Laslett, G. (1986). Thermal annealing of
 1283 fission tracks in apatite: 1. A qualitative description. *Chemical Geology: Isotope
 1284 Geoscience Section*, 59, 237–253. <https://doi.org/10/cjz3gv>
- 1285 Green, P. F., Duddy, I. R., Japsen, P., Bonow, J. M., & Malan, J. A. (2017). Post-breakup burial
 1286 and exhumation of the southern margin of Africa. *Basin Research*, 29(1), 96–127.
 1287 <https://doi.org/10/f9r64k>

- 1288 Guillocheau, F., Rouby, D., Robin, C., Helm, C., Rolland, N., Le Carlier de Veslud, C., & Braun,
1289 J. (2012). Quantification and causes of the terrigenous sediment budget at the scale of a
1290 continental margin: a new method applied to the Namibia-South Africa margin:
1291 Quantification and causes of the terrigenous sediment budget at the scale of a
1292 continental margin. *Basin Research*, 24(1), 3–30. <https://doi.org/10/bs34dc>
- 1293 Gurnis, M., Mitrovica, J. X., Ritsema, J., & Heijst, H.-J. van. (2000). Constraining mantle
1294 density structure using geological evidence of surface uplift rates: The case of the African
1295 Superplume. *Geochemistry, Geophysics, Geosystems*, 1(7). <https://doi.org/10/ck4zt8>
- 1296 Hansma, J., Tohver, E., Schrank, C., Jourdan, F., & Adams, D. (2016). The timing of the Cape
1297 Orogeny: New $^{40}\text{Ar}/^{39}\text{Ar}$ age constraints on deformation and cooling of the Cape Fold
1298 Belt, South Africa. *Gondwana Research*, 32, 122–137. <https://doi.org/10/f8n5n9>
- 1299 Hanson, E. K., Moore, J. M., Bordy, E. M., Marsh, J. S., Howarth, G., & Robey, J. V. A. (2009).
1300 CRETACEOUS EROSION IN CENTRAL SOUTH AFRICA: EVIDENCE FROM
1301 UPPER-CRUSTAL XENOLITHS IN KIMBERLITE DIATREMES. *South African*
1302 *Journal of Geology*, 112(2), 125–140. <https://doi.org/10/chqkp6>
- 1303 Hawthorne, J. (1975). Model of a kimberlite pipe. In *Physics and Chemistry of the Earth* (pp. 1–
1304 15). Elsevier.
- 1305 Hay, W. W., & Floegel, S. (2012). New thoughts about the Cretaceous climate and oceans.
1306 *Earth-Science Reviews*, 115(4), 262–272. <https://doi.org/10/gdj3z7>
- 1307 Hoggard, M. J., White, N., & Al-Attar, D. (2016). Global dynamic topography observations
1308 reveal limited influence of large-scale mantle flow. *Nature Geoscience*, 9(6), 456–463.
1309 <https://doi.org/10/f8q6vq>
- 1310 Hopkins, A. E. (2006). Seismic stratigraphic interpretation of contourite systems.
- 1311 Howard, A. D., & Kerby, G. (1983). Channel changes in badlands. *Geological Society of*
1312 *America Bulletin*, 94(6), 739–752. <https://doi.org/10/bd8c73>
- 1313 Howard, A. D., & Tierney, H. E. (2012). Taking the measure of a landscape: Comparing a
1314 simulated and natural landscape in the Virginia Coastal Plain. *Geomorphology*, 137(1),
1315 27–40. <https://doi.org/10/cmmtj3>
- 1316 Hu, J., Liu, L., Faccenda, M., Zhou, Q., Fischer, K. M., Marshak, S., & Lundstrom, C. (2018).
1317 Modification of the Western Gondwana craton by plume–lithosphere interaction. *Nature*
1318 *Geoscience*, 11(3), 203. <https://doi.org/10/gc6nb9>

- 1319 Ibbitt, R. P., Willgoose, G. R., & Duncan, M. J. (1999). Channel network simulation models
 1320 compared with data from the Ashley River, New Zealand. *Water Resources Research*,
 1321 35(12), 3875–3890. <https://doi.org/10/fhnsdp>
- 1322 Jelsma, H. A., De Wit, M. J., Thiart, C., Dirks, P. H. G. M., Viola, G., Basson, I. J., & Anckar, E.
 1323 (2004). Preferential distribution along transcontinental corridors of kimberlites and
 1324 related rocks of Southern Africa. *South African Journal of Geology*, 107(1–2), 301–324.
 1325 <https://doi.org/10/cdenp5>
- 1326 Jenkyns, H. C., Forster, A., Schouten, S., & Sinninghe Damsté, J. S. (2004). High temperatures
 1327 in the Late Cretaceous Arctic Ocean. *Nature*, 432(7019), 888–892.
 1328 <https://doi.org/10/bwk64q>
- 1329 Johnson, M. R., Van Vuuren, C. J., Hegenberger, W. F., Key, R., & Show, U. (1996).
 1330 Stratigraphy of the Karoo Supergroup in southern Africa: an overview. *Journal of*
 1331 *African Earth Sciences*, 23(1), 3–15. <https://doi.org/10/bkhkqj>
- 1332 Jourdan, F., Féraud, G., Bertrand, H., Watkeys, M., & Renne, and P. (2008). The $^{40}\text{Ar}/^{39}\text{Ar}$
 1333 ages of the sill complex of the Karoo large igneous province: Implications for the
 1334 Pliensbachian-Toarcian climate change. *Geochemistry, Geophysics, Geosystems*, 9(6).
 1335 <https://doi.org/10/b4pwmp>
- 1336 Keen-Zebert, A., Tooth, S., & Stuart, F. M. (2016). Cosmogenic ^3He Measurements Provide
 1337 Insight into Lithologic Controls on Bedrock Channel Incision: Examples from the South
 1338 African Interior. *The Journal of Geology*, 124(3), 423–434. <https://doi.org/10/gg6w2w>
- 1339 King, L. C. (1942). South African scenery. A textbook of geomorphology. *South African*
 1340 *Scenery. A Textbook of Geomorphology*.
- 1341 King, L. C. (1950). The study of the world's plainlands: a new approach in geomorphology.
 1342 *Quarterly Journal of the Geological Society*, 106(1–4), 101–131.
- 1343 Kirby, E., & Whipple, K. X. (2012). Expression of active tectonics in erosional landscapes.
 1344 *Journal of Structural Geology*, 44, 54–75. <https://doi.org/10/f4gm5d>
- 1345 Kounov, A., Niedermann, S., de Wit, M. J., Viola, G., Andreoli, M., & Erzinger, J. (2007).
 1346 Present denudation rates at selected sections of the South African escarpment and the
 1347 elevated continental interior based on cosmogenic ^3He and ^{21}Ne . *South African Journal*
 1348 *of Geology*, 110(2–3), 235–248. <https://doi.org/10/fcx8hr>

- 1349 Kounov, A., Viola, G., de Wit, M., & Andreoli, M. A. G. (2009). Denudation along the Atlantic
 1350 passive margin: new insights from apatite fission-track analysis on the western coast of
 1351 South Africa. *Geological Society, London, Special Publications*, 324(1), 287–306.
 1352 <https://doi.org/10/fg5592>
- 1353 Kounov, A., Viola, G., Dunkl, I., & Frimmel, H. E. (2013). Southern African perspectives on the
 1354 long-term morpho-tectonic evolution of cratonic interiors. *Tectonophysics*, 601, 177–191.
 1355 <https://doi.org/10/f47kxd>
- 1356 Kounov, A., Niedermann, S., De Wit, M. J., Codilean, A. T., Viola, G., Andreoli, M., & Christl,
 1357 M. (2015). COSMOGENIC ²¹Ne AND ¹⁰Be REVEAL A MORE THAN 2 Ma
 1358 ALLUVIAL FAN FLANKING THE CAPE MOUNTAINS, SOUTH AFRICA. *South
 1359 African Journal of Geology*, 118(2), 129–144. <https://doi.org/10/f7r2qq>
- 1360 Linol, B., & De Wit, M. J. (2016). *Origin and Evolution of the Cape Mountains and Karoo
 1361 Basin*. Springer.
- 1362 Lithgow-Bertelloni, C., & Silver, P. G. (1998). Dynamic topography, plate driving forces and the
 1363 African superswell. *Nature*, 395(6699), 269–272. <https://doi.org/10/fd5pfn>
- 1364 Macdonald, D., Gomez-Perez, I., Franzese, J., Spalletti, L., Lawver, L., Gahagan, L., et al.
 1365 (2003). Mesozoic break-up of SW Gondwana: implications for regional hydrocarbon
 1366 potential of the southern South Atlantic. *Marine and Petroleum Geology*, 20(3–4), 287–
 1367 308. <https://doi.org/10/dzpzhq>
- 1368 Makhubela, T. V., Kramers, J. D., Scherler, D., Wittmann, H., Dirks, P. H. G. M., & Winkler, S.
 1369 R. (2019). Effects of long soil surface residence times on apparent cosmogenic nuclide
 1370 denudation rates and burial ages in the Cradle of Humankind, South Africa. *Earth
 1371 Surface Processes and Landforms*, 44(15), 2968–2981. <https://doi.org/10/gg5s2s>
- 1372 Margirier, A., Braun, J., Gautheron, C., Carcaillet, J., Schwartz, S., Pinna Jamme, R., & Stanley,
 1373 J. (2019). Climate control on Early Cenozoic denudation of the Namibian margin as
 1374 deduced from new thermochronological constraints. *Earth and Planetary Science Letters*,
 1375 527, 115779. <https://doi.org/10/gf7tqs>
- 1376 Marsh, J., Hooper, P., Rehacek, J., Duncan, R., & Duncan, A. (1997). Stratigraphy and age of
 1377 Karoo basalts of Lesotho and implications for correlations within the Karoo igneous
 1378 province. *Geophysical Monograph-American Geophysical Union*, 100, 247–272.

- 1379 Martin, A. K., Goodlad, S. W., Hartnady, C. J. H., & Plessis, A. du. (1982). Cretaceous
 1380 palaeopositions of the Falkland Plateau relative to southern Africa using Mesozoic
 1381 seafloor spreading anomalies. *Geophysical Journal International*, 71(3), 567–579.
 1382 <https://doi.org/10/bdgqrx>
- 1383 McMillan, I. (1990). A foraminiferal biostratigraphy and chronostratigraphy for the Pliocene to
 1384 Pleistocene Upper Algoa Group, eastern Cape, South Africa. *South African Journal of*
 1385 *Geology*, 93(4), 622–622.
- 1386 Molnar, P., Houseman, G. A., & Conrad, C. P. (1998). Rayleigh—Taylor instability and
 1387 convective thinning of mechanically thickened lithosphere: effects of non-linear viscosity
 1388 decreasing exponentially with depth and of horizontal shortening of the layer.
 1389 *Geophysical Journal International*, 133(3), 568–584. <https://doi.org/10/b33r7p>
- 1390 Moore, A., & Verwoerd, W. (1985). The olivine melilitite-“kimberlite”-carbonatite suite of
 1391 Namaqualand and Bushmanland, South Africa. *Transactions of the Geological Society of*
 1392 *South Africa*, 88(2), 281–294.
- 1393 Moore, A. E. (1999). A reappraisal of epeirogenic flexure axes in southern Africa. *South African*
 1394 *Journal of Geology*, 102(4), 14.
- 1395 Moore, A. E., Blenkinsop, T., & Cotterill, F. (Woody). (2009). Southern African topography and
 1396 erosion history: plumes or plate tectonics? *Terra Nova*, 21(4), 310–315.
 1397 <https://doi.org/10/fpr3b7>
- 1398 Morgan-Wall, T. (2020). rayshader: Create Maps and Visualize Data in 2D and 3D (Version
 1399 0.15.1). Retrieved from <https://CRAN.R-project.org/package=rayshader>
- 1400 Moucha, R., & Forte, A. M. (2011). Changes in African topography driven by mantle
 1401 convection. *Nature Geoscience*, 4(10), 707–712. <https://doi.org/10/cdhgd3>
- 1402 Müller, R. D., Royer, J.-Y., & Lawver, L. A. (1993). Revised plate motions relative to the
 1403 hotspots from combined Atlantic and Indian Ocean hotspot tracks. *Geology*, 21(3), 275–
 1404 278. <https://doi.org/10/df6g42>
- 1405 Nakashole, A. N., Hodgson, D. M., Chapman, R. J., Morgan, D. J., & Jacob, R. J. (2018). Long-
 1406 term controls on continental-scale bedrock river terrace deposition from integrated clast
 1407 and heavy mineral assemblage analysis: An example from the lower Orange River,
 1408 Namibia. *Sedimentary Geology*, 364, 103–120. <https://doi.org/10/gc4fmp>

- 1409 Nunn, J. A., & Aires, J. R. (1988). Gravity anomalies and flexure of the lithosphere at the Middle
 1410 Amazon Basin, Brazil. *Journal of Geophysical Research: Solid Earth*, 93(B1), 415–428.
 1411 <https://doi.org/10/b25pdm>
- 1412 Nyblade, A. A., & Robinson, S. W. (1994). The African Superswell. *Geophysical Research*
 1413 *Letters*, 21(9), 765–768. <https://doi.org/10/fmdpkk>
- 1414 Nyblade, A. A., & Sleep, N. H. (2003). Long lasting epeirogenic uplift from mantle plumes and
 1415 the origin of the Southern African Plateau. *Geochemistry, Geophysics, Geosystems*,
 1416 4(12). <https://doi.org/10/b6xqks>
- 1417 O’Neill, C., Müller, D., & Steinberger, B. (2005). On the uncertainties in hot spot
 1418 reconstructions and the significance of moving hot spot reference frames. *Geochemistry,*
 1419 *Geophysics, Geosystems*, 6(4). <https://doi.org/10/ckb7jh>
- 1420 Osei Tutu, A., Steinberger, B., Sobolev, S. V., Rogozhina, I., & Popov, A. A. (2018). Effects of
 1421 upper mantle heterogeneities on the lithospheric stress field and dynamic topography.
 1422 *Solid Earth*, 9(3), 649–668. <https://doi.org/10/gdmt7w>
- 1423 Partridge, T. C., & Maud, R. R. (1987). Geomorphic evolution of southern Africa since the
 1424 Mesozoic. *South African Journal of Geology*, 90(2), 179–208.
- 1425 Partridge, T. C., Dollar, E. S. J., Moolman, J., & Dollar, L. H. (2010). The geomorphic provinces
 1426 of South Africa, Lesotho and Swaziland: A physiographic subdivision for earth and
 1427 environmental scientists. *Transactions of the Royal Society of South Africa*, 65(1), 1–47.
 1428 <https://doi.org/10/b8vz9j>
- 1429 Paul, J. D., Roberts, G. G., & White, N. (2014). The African landscape through space and time.
 1430 *Tectonics*, 33(6), 898–935. <https://doi.org/10/f6ct3s>
- 1431 Pérez-Gussinyé, M., Metois, M., Fernández, M., Vergés, J., Fullea, J., & Lowry, A. R. (2009).
 1432 Effective elastic thickness of Africa and its relationship to other proxies for lithospheric
 1433 structure and surface tectonics. *Earth and Planetary Science Letters*, 287(1), 152–167.
 1434 <https://doi.org/10/ftfcqp>
- 1435 Phillips, D., & Harris, J. W. (2009). Diamond provenance studies from ⁴⁰Ar/³⁹Ar dating of
 1436 clinopyroxene inclusions: An example from the west coast of Namibia. *Lithos*, 112, 793–
 1437 805. <https://doi.org/10/bcrxhs>

- 1438 Phillips, D., Harris, J. W., de Wit, M. C. J., & Matchan, E. L. (2018). Provenance history of
 1439 detrital diamond deposits, West Coast of Namaqualand, South Africa. *Mineralogy and*
 1440 *Petrology*, *112*(S1), 259–273. <https://doi.org/10/gg6wp7>
- 1441 Pickford, M., Eisenmann, V., & Senut, B. (1999). Timing of landscape development and calcrete
 1442 genesis in northern Namaqualand, South Africa, 3.
- 1443 Ponte, J.-P., Robin, C., Guillocheau, F., Popescu, S., Suc, J.-P., Dall’Asta, M., et al. (2019). The
 1444 Zambezi delta (Mozambique channel, East Africa): High resolution dating combining
 1445 bio- orbital and seismic stratigraphies to determine climate (palaeoprecipitation) and
 1446 tectonic controls on a passive margin. *Marine and Petroleum Geology*, *105*, 293–312.
 1447 <https://doi.org/10/gg2pjb>
- 1448 Pysklywec, R. N., & Mitrovica, J. X. (1999). The Role of Subduction-Induced Subsidence in the
 1449 Evolution of the Karoo Basin. *The Journal of Geology*, *107*(2), 155–164.
 1450 <https://doi.org/10/fjc5r7>
- 1451 Raab, M. J., Brown, R. W., Gallagher, K., Carter, A., & Weber, K. (2002). Late Cretaceous
 1452 reactivation of major crustal shear zones in northern Namibia: constraints from apatite
 1453 fission track analysis. *Tectonophysics*, *349*(1–4), 75–92. <https://doi.org/10/cd5b3t>
- 1454 Raab, M. J., Brown, R. W., Gallagher, K., Weber, K., & Gleadow, A. J. W. (2005). Denudational
 1455 and thermal history of the Early Cretaceous Brandberg and Okenyenya igneous
 1456 complexes on Namibia’s Atlantic passive margin: EXHUMATION OF NAMIBIA’S
 1457 PASSIVE MARGIN. *Tectonics*, *24*(3), n/a-n/a. <https://doi.org/10/c6sgsg>
- 1458 Rayner, R. J., Bamford, M. K., Brothers, D. J., Dippenaar-Schoeman, A. S., McKay, I. J.,
 1459 Oberprieler, R. G., & Waters, S. B. (1997). CRETACEOUS FOSSILS FROM THE
 1460 ORAPA DIAMOND MINE. *Palaeont. Afr.*, *33*, 55–65.
- 1461 Renne, P. R., Glen, J. M., Milner, S. C., & Duncan, A. R. (1996). Age of Etendeka flood
 1462 volcanism and associated intrusions in southwestern Africa. *Geology*, *24*(7), 659–662.
 1463 <https://doi.org/10/c4h9kz>
- 1464 Richardson, J. C., Hodgson, D. M., Paton, D., Craven, B., Rawcliffe, A., & Lang, A. (2017).
 1465 Where is my sink? Reconstruction of landscape development in southwestern Africa
 1466 since the Late Jurassic. *Gondwana Research*, *45*, 43–64. <https://doi.org/10/f9zhv6>
- 1467 Roberts, D. L., Sciscio, L., Herries, A. I., Scott, L., Bamford, M. K., Musekiwa, C., & Tsikos, H.
 1468 (2013). Miocene fluvial systems and palynofloras at the southwestern tip of Africa:

- 1469 Implications for regional and global fluctuations in climate and ecosystems. *Earth-*
 1470 *Science Reviews*, 124, 184–201. <https://doi.org/10/f494kc>
- 1471 Roberts, E. M., Stevens, N. J., O’Connor, P. M., Dirks, P. H. G. M., Gottfried, M. D., Clyde, W.
 1472 C., et al. (2012). Initiation of the western branch of the East African Rift coeval with the
 1473 eastern branch. *Nature Geoscience*, 5(4), 289–294. <https://doi.org/10/mhn>
- 1474 Roberts, G. G., & White, N. (2010). Estimating uplift rate histories from river profiles using
 1475 African examples. *Journal of Geophysical Research: Solid Earth*, 115(B2).
 1476 <https://doi.org/10/b3wrqz>
- 1477 Rouby, D., Bonnet, S., Guillocheau, F., Gallagher, K., Robin, C., Biancotto, F., et al. (2009).
 1478 Sediment supply to the Orange sedimentary system over the last 150My: An evaluation
 1479 from sedimentation/denudation balance. *Marine and Petroleum Geology*, 26(6), 782–794.
 1480 <https://doi.org/10/bm25dp>
- 1481 Rubey, M., Brune, S., Heine, C., Davies, D. R., Williams, S. E., & Müller, R. D. (2017). Global
 1482 patterns in Earth’s dynamic topography since the Jurassic: the role of subducted slabs.
 1483 *Solid Earth*, 8(5), 899–919. <https://doi.org/10/gcdj76>
- 1484 Rudge, J. F., Roberts, G. G., White, N. J., & Richardson, C. N. (2015). Uplift histories of Africa
 1485 and Australia from linear inverse modeling of drainage inventories: RUDGE ET AL.
 1486 *Journal of Geophysical Research: Earth Surface*, 120(5), 894–914.
 1487 <https://doi.org/10/gg6wn3>
- 1488 Said, A., Moder, C., Clark, S., & Ghorbal, B. (2015). Cretaceous–Cenozoic sedimentary budgets
 1489 of the Southern Mozambique Basin: Implications for uplift history of the South African
 1490 Plateau. *Journal of African Earth Sciences*, 109, 1–10. <https://doi.org/10/f7mvxb>
- 1491 Sambridge, M. (1999). Geophysical inversion with a neighbourhood algorithm—I. Searching a
 1492 parameter space. *Geophysical Journal International*, 138(2), 479–494.
 1493 <https://doi.org/10/b84mkr>
- 1494 Sandersen, A. (2007). *A palynological investigation of the offshore Cretaceous sequence on the*
 1495 *south-west coast of South Africa* (PhD). University of the Witwatersrand, Johannesburg,
 1496 South Africa.
- 1497 Scharf, T. E., Codilean, A. T., Wit, M. de, Jansen, J. D., & Kubik, P. W. (2013). Strong rocks
 1498 sustain ancient postorogenic topography in southern Africa. *Geology*, 41(3), 331–334.
 1499 <https://doi.org/10/f23vp5>

- 1500 Scheiber-Enslin, S. E., Ebbing, J., & Webb, S. J. (2015). NEW DEPTH MAPS OF THE MAIN
1501 KAROO BASIN, USED TO EXPLORE THE CAPE ISOSTATIC ANOMALY, SOUTH
1502 AFRICA. *South African Journal of Geology*, *118*(3), 225–248. <https://doi.org/10/f72b79>
- 1503 Schmitz, M. D., & Bowring, S. A. (2003). Constraints on the thermal evolution of continental
1504 lithosphere from U-Pb accessory mineral thermochronometry of lower crustal xenoliths,
1505 southern Africa. *Contributions to Mineralogy and Petrology*, *144*(5), 592–618.
1506 <https://doi.org/10/dpp9sd>
- 1507 Scholtz, A. (1985). The palynology of the upper lacustrine sediments of the Arnot Pipe, Banke,
1508 Namaqualand. *Annals of the South African Museum*, *95*(1), 1–109.
- 1509 Senut, B., Pickford, M., & Ségalen, L. (2009). Neogene desertification of Africa. *Comptes*
1510 *Rendus Geoscience*, *341*(8), 591–602. <https://doi.org/10/c8zb7x>
- 1511 Shuster, D. L., Flowers, R. M., & Farley, K. A. (2006). The influence of natural radiation
1512 damage on helium diffusion kinetics in apatite. *Earth and Planetary Science Letters*,
1513 *249*(3), 148–161. <https://doi.org/10/c6nkx5>
- 1514 Skinner, C. J., Coulthard, T. J., Schwanghart, W., Wiel, M. J. V. D., & Hancock, G. (2018).
1515 Global sensitivity analysis of parameter uncertainty in landscape evolution models.
1516 *Geoscientific Model Development*, *11*(12), 4873–4888. <https://doi.org/10/ggxjsd>
- 1517 Smith, R. (1986). Sedimentation and palaeoenvironments of Late Cretaceous crater-lake deposits
1518 in Bushmanland, South Africa. *Sedimentology*, *33*(3), 369–386. <https://doi.org/10/djrj8v3>
- 1519 Stanley, J. R. (2020). Model inputs and results from FastScape landscape evolution model runs
1520 for southern Africa [Data set]. Zenodo. <http://doi.org/10.5281/zenodo.4153803>
- 1521 Stanley, J. R., & Flowers, R. M. (2020). Mesozoic denudation history of the lower Orange River
1522 and eastward migration of erosion across the southern African Plateau. *Lithosphere*.
1523 <https://doi.org/10/ggjt45>
- 1524 Stanley, J. R., Flowers, R. M., & Bell, D. R. (2013). Kimberlite (U-Th)/He dating links surface
1525 erosion with lithospheric heating, thinning, and metasomatism in the southern African
1526 Plateau. *Geology*, *41*(12), 1243–1246. <https://doi.org/10/f5pbr9>
- 1527 Stanley, J. R., Flowers, R. M., & Bell, D. R. (2015). Erosion patterns and mantle sources of
1528 topographic change across the southern African Plateau derived from the shallow and
1529 deep records of kimberlites. *Geochemistry, Geophysics, Geosystems*, *16*(9), 3235–3256.
1530 <https://doi.org/10/f7zgxb>

- 1531 Steinberger, B. (2016). Topography caused by mantle density variations: observation-based
1532 estimates and models derived from tomography and lithosphere thickness. *Geophysical*
1533 *Journal International*, 205(1), 604–621. <https://doi.org/10/gg3h64>
- 1534 Steinberger, B., & Torsvik, T. H. (2008). Absolute plate motions and true polar wander in the
1535 absence of hotspot tracks. *Nature*, 452(7187), 620–623. <https://doi.org/10/c4pvr4>
- 1536 Steinberger, B., Conrad, C. P., Osei Tutu, A., & Hoggard, M. J. (2019). On the amplitude of
1537 dynamic topography at spherical harmonic degree two. *Tectonophysics*, 760, 221–228.
1538 <https://doi.org/10/ggzvt9>
- 1539 Stevenson, I. R., & McMillan, I. K. (2004). Incised valley fill stratigraphy of the Upper
1540 Cretaceous succession, proximal Orange Basin, Atlantic margin of southern Africa.
1541 *Journal of the Geological Society*, 161(2), 185–208. <https://doi.org/10/dp5bzq>
- 1542 Summerfield, M. A. (1983). Silcrete as a palaeoclimatic indicator: evidence from southern
1543 Africa. *Palaeogeography, Palaeoclimatology, Palaeoecology*, 41(1), 65–79.
1544 <https://doi.org/10/fmn95k>
- 1545 Svensen, H., Corfu, F., Polteau, S., Hammer, Ø., & Planke, S. (2012). Rapid magma
1546 emplacement in the Karoo Large Igneous Province. *Earth and Planetary Science Letters*,
1547 325–326, 1–9. <https://doi.org/10/gg6wvq>
- 1548 Tennekes, M. (2018). tmap: Thematic Maps in R. *Journal of Statistical Software*, 84(6), 1–39.
1549 <https://doi.org/10/gfdd6z>
- 1550 Thiéblemont, A., Hernandez-Molina, F. J., Ponte, J.-P., Robin, C., Guillocheau, F., Cazzola, C.,
1551 & Raison, F. (2020). Seismic stratigraphic framework and depositional history for
1552 Cretaceous and Cenozoic contourite depositional systems of the Mozambique Channel,
1553 SW Indian Ocean. *Marine Geology*, 425, 106192. <https://doi.org/10/ghdn67>
- 1554 Tinker, J., de Wit, M., & Brown, R. W. (2008a). Linking source and sink: Evaluating the balance
1555 between onshore erosion and offshore sediment accumulation since Gondwana break-up,
1556 South Africa. *Tectonophysics*, 455(1–4), 94–103. <https://doi.org/10/ctp34n>
- 1557 Tinker, J., de Wit, M., & Brown, R. W. (2008b). Mesozoic exhumation of the southern Cape,
1558 South Africa, quantified using apatite fission track thermochronology. *Tectonophysics*,
1559 455(1–4), 77–93. <https://doi.org/10/dw26sb>

- 1560 Uenzelmann-Neben, G., Schlüter, P., & Weigelt, E. (2007). Cenozoic oceanic circulation within
1561 the South African gateway: indications from seismic stratigraphy. *South African Journal*
1562 *of Geology*, 110(2–3), 275–294. <https://doi.org/10/ctvbzj>
- 1563 Van Der Beek, P., Summerfield, M. A., Braun, J., Brown, R. W., & Fleming, A. (2002).
1564 Modeling postbreakup landscape development and denudational history across the
1565 southeast African (Drakensberg Escarpment) margin. *Journal of Geophysical Research:*
1566 *Solid Earth*, 107(B12), ETG 11-1-ETG 11-18. <https://doi.org/10/cx7qnx>
- 1567 Watkins, C. E., & Conrad, C. P. (2018). Constraints on dynamic topography from asymmetric
1568 subsidence of the mid-ocean ridges. *Earth and Planetary Science Letters*, 484, 264–275.
1569 <https://doi.org/10/gc25h7>
- 1570 Whipple, K. X. (2004). Bedrock Rivers and the Geomorphology of Active Orogens. *Annual*
1571 *Review of Earth and Planetary Sciences*, 32(1), 151–185. <https://doi.org/10/dwkzhq>
- 1572 Whipple, K. X., & Tucker, G. E. (1999). Dynamics of the stream-power river incision model:
1573 Implications for height limits of mountain ranges, landscape response timescales, and
1574 research needs. *Journal of Geophysical Research: Solid Earth*, 104(B8), 17661–17674.
1575 <https://doi.org/10/brj8r8>
- 1576 Wickham, H. (2016). *ggplot2: Elegant Graphics for Data Analysis*. New York: Springer-Verlag.
1577 Retrieved from <https://ggplot2.tidyverse.org>
- 1578 Wildman, M., Brown, R. W., Watkins, R., Carter, A., Gleadow, A., & Summerfield, M. (2015).
1579 Post break-up tectonic inversion across the southwestern cape of South Africa: New
1580 insights from apatite and zircon fission track thermochronometry. *Tectonophysics*, 654,
1581 30–55. <https://doi.org/10/f7knvj>
- 1582 Wildman, M., Brown, R. W., Beucher, R., Persano, C., Stuart, F., Gallagher, K., et al. (2016).
1583 The chronology and tectonic style of landscape evolution along the elevated Atlantic
1584 continental margin of South Africa resolved by joint apatite fission track and (U-Th-
1585 Sm)/He thermochronology: Evolution of SW African Passive Margin. *Tectonics*, 35(3),
1586 511–545. <https://doi.org/10/bcvn>
- 1587 Wildman, M., Brown, R., Persano, C., Beucher, R., Stuart, F. M., Mackintosh, V., et al. (2017).
1588 Contrasting Mesozoic evolution across the boundary between on and off craton regions
1589 of the South African plateau inferred from apatite fission track and (U-Th-Sm)/He

- 1590 thermochemistry: Mesozoic Evolution of Southern Africa. *Journal of Geophysical*
1591 *Research: Solid Earth*, 122(2), 1517–1547. <https://doi.org/10/f9t9zx>
- 1592 Williams, L. S. (2015). Sedimentology of the Lower Cretaceous reservoirs of the Sea Lion Field,
1593 North Falkland Basin. *Petroleum Geoscience*, 21(2–3), 183–198.
1594 <https://doi.org/10/gg6w4n>
- 1595 Winterbourne, J., Crosby, A., & White, N. (2009). Depth, age and dynamic topography of
1596 oceanic lithosphere beneath heavily sedimented Atlantic margins. *Earth and Planetary*
1597 *Science Letters*, 287(1–2), 137–151. <https://doi.org/10/bv97vs>
- 1598 de Wit, M. C. J. (1999). Post-Gondwana drainage and the development of diamond placers in
1599 western South Africa. *Economic Geology*, 94(5), 721–740. <https://doi.org/10/fsz8gz>
- 1600 de Wit, M. (2007). The Kalahari Epeirogeny and climate change: differentiating cause and effect
1601 from core to space. *South African Journal of Geology*, 110(2–3), 367–392.
1602 <https://doi.org/10/bqc7x2>
- 1603 Zhang, N., Zhong, S., & Flowers, R. M. (2012). Predicting and testing continental vertical
1604 motion histories since the Paleozoic. *Earth and Planetary Science Letters*, 317–318, 426–
1605 435. <https://doi.org/10/bhrqhr>
1606
1607